Photon Counting CT For Ultra Low-Dose Lung Cancer Screening

A Phantom Study

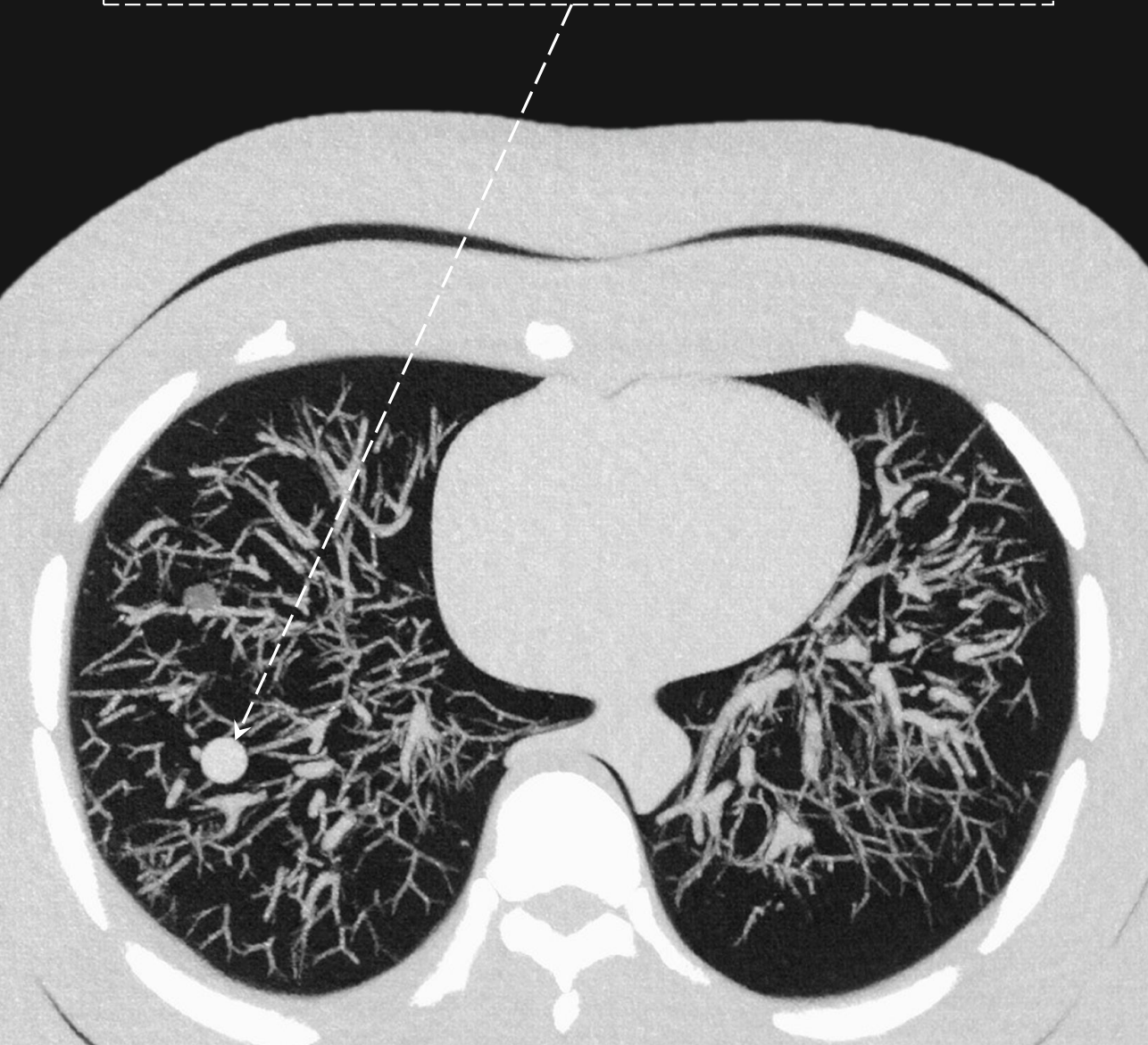

Technical Medicine
MSc. thesis by Anna Walstra
June 2023

Photon Counting CT for Ultra Low-Dose Lung Cancer Screening

A PHANTOM STUDY

by

Anna Noëlle Hillary WALSTRA

Student number: 4543653

9th June, 2023

Thesis in partial fulfilment of the requirements for the joint degree of Master of Science in

Technical Medicine

Leiden University | Delft University of Technology | Erasmus University Rotterdam

Master thesis project (TM30004, 35 ECTS)
Dept. of Radiology, University Medical Center Groningen
November 2022 – June 2023

Supervisors:	
Prof. dr. Rozemarijn Vliegenthart	UMC Groningen
Dr. ir. Marcel van Straten	Erasmus MC
Dr. Marcel Greuter	UMC Groningen
Dr. Niels Schurink	Siemens-Healthineers

Thesis committee members:	
Dr. ir. Theo van Walsum (chair)	Erasmus MC
Dr. Wouter Veldkamp	Leiden UMC
Prof. dr. Rozemarijn Vliegenthart	UMC Groningen
Dr. ir. Marcel van Straten	Erasmus MC

Universiteit Leiden

TU Delft Delft University of Technology

ERASMUS UNIVERSITEIT ROTTERDAM

CONTENTS

ABSTRACT

Objective: The two-fold aim of this phantom study was first to evaluate the accuracy of pulmonary nodule detection for lung cancer screening at progressively lower dose levels of photon-counting computed tomography (PC-CT) and, second, to objectively compare the image quality across different acquisition and reconstruction settings, through a comparison of PC-CT and conventional energy-integrating detector (EID) CT.

Methods: Thirty-six artificial lung nodules with 6 diameters (2.5, 3, 4, 5, 6 and 10 mm), 3 shapes (spherical, lobulated, spiculated) and two densities (-300 HU and +100 HU) were placed in an anthropomorphic chest phantom. The phantom was scanned using a standard lung cancer screening protocol (Sn 100 kV) with dose-matched EID-CT and PC-CT ($CTDI_{vol}$ of 0.8 mGy), in addition to 75%, 50%, 25% and 10% doses on the PC-CT ($CTDI_{vol}$ 0.6-0.07 mGy). Nodule detection was performed by one experienced reader, and denoted as the sensitivity, specificity, precision and false positive (FP) nodules. The acquisitions for assessing image quality were performed on a Quality Assurance (QA) phantom at full dose, with varying levels of iterative reconstruction (IR), virtual monoenergetic image (VMI) keV levels, slice thicknesses and increments, kernel strengths and scan modes. The noise power spectrum (NPS) and the task-based transfer function (TTF) were computed. The detectability index (d') was computed to model the detection of a 4 mm solid and 5 mm subsolid pulmonary nodule.

Results: Sensitivity of 58%, 59%, 62%, 55%, 51% and specificity of 95%, 90%, 80%, 75%, 50% were obtained at 100%, 75%, 50%, 25% and 10% doses on the PC-CT, respectively, compared to the 59% sensitivity and 100% specificity on the EID-CT. The precision was 100% on the EID-CT and 94-99% on the PC-CT down to 25% dose, whereas at 10% dose the precision dropped to 88% and the FP nodules tripled from 5 to 15. Increasing the IR level, VMI keV and slice thickness substantially decreased noise magnitude, with only minimal changes in noise texture. In contrast, higher kernel strength increased the noise magnitude, but created a finer noise texture. All settings showed a minimal impact on the spatial resolution. Noise magnitude was 40-60% higher on the EID-CT compared to PC-CT for all scan modes, although no difference in spatial resolution was found. Furthermore, the PC-CT attained 30-50% higher d' values independent of scan mode or tin filter, in comparison to the EID-CT at a similar dose.

Conclusion: PC-CT with similar acquisition and reconstruction settings demonstrated comparable sensitivity for lung nodule detection despite lower radiation dose, when compared with EID-CT for low-dose lung cancer CT screening. However, attention has to be paid to FP findings at ultra-low dose levels, since the specificity decreased with every dose reduction. Furthermore, PC-CT achieved higher d' values compared to EID-CT at an equivalent dose, through enhanced image quality and less noise. Additionally, the study shows that optimizing the image acquisition and reconstruction parameters can further enhance the image quality of PC-CT. These findings show that PC-CT holds significant promise as an alternative method for low-dose lung cancer screening. Consequently, future research should focus on evaluating the performance of PC-CT further on a more representative anthropomorphic phantom and in a clinical setting.

ABBREVIATIONS

Abbreviation	Definition
Bl	Lung kernel
Br	Body kernel
CNR	Contrast-to-noise ratio
CT	Computed Tomography
CTDIvol	Volume CT dose index
d'	Detectability index
Dw	Water equivalent diameter
EID	Energy-integrating detector
ESF	Edge spread function
FOV	Field-of-view
FP	False positive
f_{peak}	Peak frequency
FPR	False positive rate
HU	Hounsfield unit
IQ	Image quality level
IR	Iterative reconstruction
LD	Low dose
LSF	Line-spread function
MIP	Maximum Intensity Projection
NELSON	The Dutch-Belgian Randomized Lung Cancer Screening Trial
NLST	National Lung Screening Trial
NPS	Noise power spectrum
PC	Photon-counting
Q+	Quantum plus mode (120 kV)
QIR	Quantum iterative reconstruction
Qr	Quantitative kernel
QRM	Quality reference mAs
QSn	Quantum mode (100 kV) with tin filter
TN	True negative
TP	True positive
TTF	Task-based transfer function
UHR	Ultra-high resolution
ULD	Ultra-low dose
VMI	Virtual monoenergetic image

1

INTRODUCTION

LUNG cancer is a major health concern, being the second most commonly diagnosed cancer and accounting for 11.4% of all new cancer cases and 18.0% of all cancer deaths [1]. The low survival rate of lung cancer can be attributed to the detection at an advanced stage [2]. Chest radiography and sputum cytology have been found to be ineffective screening tests through controlled trials. However, the use of computed tomography (CT) for screening has shown a significant reduction in lung cancer mortality [3]. The volume, shape and growth of the nodules are characteristic markers for malignancy [4, 5]. In long-term smokers screening showed to reduce lung cancer mortality by 20-24%, supported by results from two adequately sized trials: the American National Lung Screening Trial (NLST) and The Dutch-Belgian Randomized Lung Cancer Screening Trial (NELSON) [6, 7]. The current screening protocols suggest an annual or biennial frequency for adequate screening of high risk patients, considering the cost-effectiveness and mortality reduction [8–11]. However, this frequency of CT scans over a lifetime raises concerns for the induced cancer risk of repeated screening [8, 12]. Especially since the cumulative medical radiation exposure increased in recent years, due to the wider application of CT imaging in clinical practice [12].

To mitigate these concerns, low-dose (LD) and ultra-low dose (ULD) CT protocols have been developed through the optimization of CT protocols and technological advancements. A review on (U)LD CT techniques showed that accurate detection and quantification of pulmonary nodules is feasible, although advanced iterative reconstruction (IR) techniques were necessary to achieve the required diagnostic quality [13]. The NLST and NELSON trials were the first large studies for lung cancer screening and used LD CT protocols [6, 7]. Although these techniques have shown promise in accurately detecting and quantifying pulmonary nodules, there remains a wide range in radiation dose and variations in image acquisition that may impact the reliability of multiple screening rounds [14–17].

Recently, a new CT technology called photon-counting CT has been introduced to the market. A scanner with such technology is equipped with photon-counting (PC) detectors instead of the conventional energy-integrating detectors (EID). This system allows for the measurement of the incident energy of photons in the X-ray beam, as well as the counting of individual photons. PC-CT directly converts the X-ray photons to electrical signal, whereas in EID-CT a two-step conversion process is required. First, the X-ray photons are converted to visible light in the scintillation crystal, after which the light is converted to an electrical signal by a photodiode. The spectral information of the incoming signal is lost during the accumulation and measurement of the light over the integration time. Another limitation is that lower energy X-rays are down-weighted in EID-CT compared to the high energy X-rays. In PC-CT all X-rays above a certain energy threshold contribute equally to the measurement signal, and signals below the

energy threshold are removed [18, 19]. The direct signal conversion and noise reduction of the PC detectors can increase the dose efficiency. Moreover, the reflection septa in EID are not required in PC detectors, removing the dead space and creating smaller detector pixels without compromising geometric detection efficiency. Moreover, the reduced pixel size of PC detectors enable ultra-high resolution (UHR) imaging as well as the advantage of obtaining routine imaging at lower radiation doses. Hence, the increased dose efficiency and improved image quality of PC-CT can lead to enhanced diagnostic accuracy in detecting and quantifying pulmonary nodules at a minimal exposure level. Initial studies on PC-CT have shown promising results for detecting and quantifying pulmonary nodules at lower dose levels, though further research is needed to fully assess its effectiveness in comparison to conventional EID-CT in lung cancer screening [18–22]. Optimal dose levels for lung cancer screening have not been established yet.

Therefore, the objective of this phantom study was to evaluate the accuracy of pulmonary nodule detection at progressively lower dose levels and, second, to objectively compare the image quality across different acquisition and reconstruction settings, through a comparison of PC-CT and conventional EID-CT.

2

MATERIALS AND METHODS

2.1. PHANTOMS AND NODULES

2.1.1. LUNGMAN PHANTOM

An anthropomorphic thorax phantom (Lungman phantom, Kyoto Kagaku Co., Ltd., Kyoto, Japan) was used to evaluate the pulmonary nodule detection at different dose levels. The phantom is an accurate life-size anatomical model of a male human torso with arms in abducted position (figure 2.1). The lungs are simulated by air naturally in the phantom, where the bronchi and pulmonary vessels are simulated by a mesh structure connected to the mediastinum. Artificial nodules can be attached to any arbitrary structure in the lung field. Phantom specifications are as follows: 43 cm (width) x 20 cm (depth) x 46 cm (height), phantom weight 18 kg, water equivalent diameter (Dw) of 23.6 cm [23]. Additional chest plates were attached to the phantom to simulate a larger body type (Dw 29.9 cm) and approach the average human body of approximately 80 kg [24].

A total of thirty-six artificial nodules were 3D printed in-house, ranging in size (2.5, 3, 4, 5, 6 and 10 mm), attenuation (subsolid (~-300 Hounsfield Unit (HU)) and solid (~+100 HU)) and shape (spherical, lobulated, spiculated) (figure 2.3). The nodules were spread in the Lungman lungs according to a randomized scheme, automatically created by an in-house developed script. All nodules were included three times, in a total of sixteen different setups. Four additional acquisitions were acquired with no artificial nodules. Thus, a total of twenty nodule setups, where 20% contained no nodules, were scanned with the EID-CT and PC-CT protocols (section 2.2, table 2.1). The complete nodule placement schemes can be found in Appendix *A* for both the EID-CT and PC-CT.

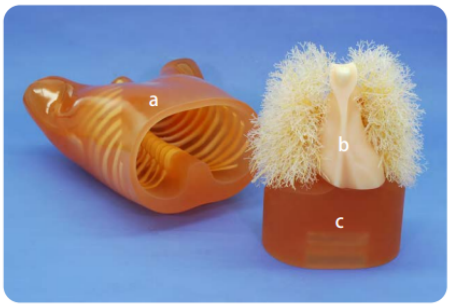

Figure 2.1: Lungman phantom with the (a) main body (chest wall), (b) lungs and mediastinum (incl. heart and trachea and (c) the abdomen block *[23]*.

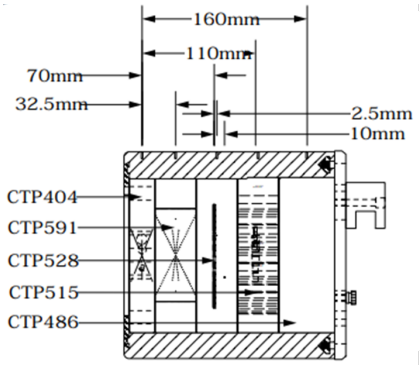

Figure 2.2: Catphan 600 phantom longitudinal cross section displaying the different modules, with the CTP404 Sensitometry Module and CTP486 homogeneous module used for spatial resolution and noise calculation, respectively *[25]*.

Figure 2.3: A. Artificial nodules situated in the lungs of the Lungman phantom, solid nodules were reflective with UV light. B. Lungs placed within the Lungman thorax. C. Overview of the artificial nodules, with different shapes, sizes and densities (Red/blue = subsolid -300 HU, White/Clear = solid +100 HU).

2.1.2. CATPHAN PHANTOM

Quantitative image quality measurements were performed using the Catphan 600 phantom (The Phantom Laboratory, Salem NY, USA), which is specifically designed for testing the image quality of CT scanners. The Catphan consists of five modules enclosed in a 20cm housing [25]. The CTP404 Sensitometry Module (section 1) contains inserts made of air, polymethylpentene (PMP), low-density polyethylene (LDPE), polystyrene, acrylic, delrin, and teflon, as well as a small vial which can be filled with water and inserted into the top hole of the module. Through an evaluation of the CTP404 module and analyzing the inserts that closely resemble the contrast of lesions observed in clinical practice, it is possible to determine the spatial resolution. The CTP486 Image Uniformity Module (section 5) with CT numbers within 2% of water's density at standard scanning protocols, was used to evaluate image noise and image uniformity. The CTP404 and CTP486 modules were used for calculation of the Task-based Transfer Function (TTF) and the Noise Power Spectrum (NPS), respectively (section 2.5).

2.2. CT ACQUISITION

2.2.1. CONVENTIONAL EID-CT

Two standard lung cancer screening protocols with and without tin filter, according to the current screening protocol recommendations, served as a reference for diagnostic quality [6, 7]. The phantoms were scanned on a conventional EID-CT system currently used for lung cancer imaging (SOMATOM Force, Siemens Healthcare GmbH, Erlangen, Germany) with a 1.2 pitch (0.5 s rotation time) and detector configuration of 192 × 0.6 mm. The tube voltage was set to Sn100 kVp (including 0.6 mm tin filter) and 120 kVp. The Lungman phantom scans were performed at $CTDI_{vol}$ levels of 0.79 mGy (Sn100 kVp) and 1.46 mGy (120 kVp) with automatic exposure control (CARE Dose4D; Siemens Healthcare GmbH, Erlangen, Germany) turned on. The tin filter reduces the number of photons over the entire energy range, especially the low-energy photons, hence a higher quality reference mAs (QRM) was required (table 2.1).

The Catphan phantom scans were obtained with similar acquisition settings (Sn100 kVp / 120 kVp) at $CTDI_{vol}$ levels of 0.55 mGy (Sn100 kVp) and 0.56 mGy (120 kVp) with CARE Dose4D turned off. The $CTDI_{vol}$ levels were set to match the lowest dose for an average patient pro-

Table 2.1: Parameters for CT Acquisition and Reconstruction

Modality	**EID-CT**		**PC-CT**
Beam collimation [mm]	96 x 0.6		144 x 0.4
kVp	Sn 100	120	Sn 100
QRM or IQ level *(Lungman / Catphan)*	187 / 130 (QRM)	23 / 8 (QRM)	12, 9, 6, 3, 1 / 65 (IQ level)
CTDIvol [mGy] *(Lungman / Catphan)*	0.79 / 0.55	1.45 / 0.56	0.81, 0.61, 0.41, 0.20, 0.07 / 0.55
Rotation time [s]	0.5		0.5
Pitch	1.2		1.2
FOV [mm]	300		300
Scan length [mm] *(Lungman / Catphan)*	300 / 214		300 / 204
Iterative reconstruction	ADMIRE-3		QIR-3
Matrix size	512 x 512		Auto 512 x 512 (Br40) 768 x 768 (Bl56, Qr60)
Reconstruction kernel	Br40, Bl57, Qr59		Br40, Bl56, Qr60
Slice thickness/increment [mm]	1.0/0.7		1.0/0.7
Spectral reconstruction	n.a.		VMI 70 keV

CT, computed tomography; PC, photon-counting; EID, energy-integrating detector; $CTDI_{vol}$, CT dose index-volume; QRM, quality reference mAs; IQ, image quality level; QIR, quantum iterative reconstruction; FOV, field-of-view.

vided by the AAPM Lung Cancer Screening Protocols 2019 [24], since the Dw value of the Catphan phantom is lower compared to the Lungman phantom with chest plates (Dw 19.6 / 29.6 ≈ $CTDI_{vol}$ 0.55 / 0.8). The Catphan scans were repeated five times, to evaluate the uncertainty associated with the image quality metrics (section 2.5).

2.2.2. PHOTON-COUNTING CT

The Lungman phantom was scanned separately on a commercially available, clinical PC-CT system (NAEOTOM Alpha, Siemens Healthcare GmbH, Erlangen, Germany) with a 1.2 pitch and detector configuration of 144 x 0.4 mm. The optimal matrix size was automatically selected (Precision Matrix; Siemens Healthcare GmbH, Erlangen, Germany), taking the reconstruction kernel and field-of-view (FOV) into account. First, the Lungman phantom was scanned with similar acquisition settings and dose level to the EID-CT Sn100 kVp protocol. The dose was matched by adjusting the image quality (IQ) level of CARE Dose4D. Hereafter, the dose was lowered to 75/50/25/10% of the reference EID-CT $CTDI_{vol}$.

The different scan modes were investigated using both the Lungman and Catphan phantom. Specifically for these scans the Lungman phantom contained all artificial nodules, instead of varying nodule setups, to investigate the nodule volumetry using different scan modes in a later stage of the study. Initially, the standard tin protocol (QSn mode; Sn100 kVp) served as the baseline and was repeated five times on the Catphan phantom, to evaluate the uncertainty associated with the image quality metrics (section 2.5). Hereafter, three different scan modes (Q+, UHR Q+, UHR QSn) were applied, details in table 2.2. See section 2.3 for the fifteen different reconstruction settings of the baseline scan.

2.3. IMAGE RECONSTRUCTION

The standard reconstruction parameters for all images are shown in table 2.1 and 2.2. The EID-CT images were reconstructed similar to clinical practice, with a Br40 kernel for the pulmonary

Table 2.2: Parameters for PC-CT Acquisition and Reconstruction for image quality evaluation.

Scan mode	**Quantum Sn (standard)**		**Quantum+**	**UHR Quantum Sn**	**UHR Quantum+**
Beam collimation [mm]	144 x 0.4		144 x 0.4	120 x 0.2	120 x 0.2
kVp	Sn 100		120	Sn 100	120
IQ level *(Lungman / Catphan)*	12 / 65		12 / 7	13 / 65	10 / 7
CTDIvol [mGy] *(Lungman / Catphan)*	0.82 / 0.55		0.85 / 0.55	0.82 / 0.56	0.78 / 0.56
FOV [mm]	300		300	300	300
Scan length [mm] *(Lungman / Catphan)*	300 / 204		300 / 204	300 / 204	300 / 204
Reconstruction settings	*Standard*	*Alternative*			
Iterative reconstruction	QIR 3	QIR 1, 2, 4	QIR 3	QIR 3	QIR 3
Matrix size	Auto	512x512, 768x768, 1024x1024	Auto	Auto	Auto
Reconstruction kernel	Br40, Bl56, Qr60	Br36, Br44, Bl60, Bl64, Qr76	Br40, Bl56, Qr60	Br40, Bl56, Qr56, Qr60, Qr76, Qr89	Br40, Bl56, Qr56, Qr60, Qr76, Qr89
Slice thickness/ increment [mm]	1.0/0.7	0.8/0.6, 0.6/0.4, 0.4/0.2	1.0/0.7	0.4/0.2 0.2/0.1 (Qr89)	0.4/0.2 0.2/0.1 (Qr89)
Spectral reconstruction	VMI 70 keV	VMI 60, 65, 80, 90 keV	VMI 70 keV	VMI 70 keV Auto keV (Qr89)	VMI 70 keV Auto keV (Qr89)

CT, computed tomography; PC, photon-counting; $CTDI_{vol}$, CT dose index-volume; IQ, Image Quality level; QIR, quantum iterative reconstruction; FOV, field-of-view; VMI, virtual monoenergetic image; UHR, ultra-high resolution

nodule detection, Bl57/Qr59 for the volume measurements, using the IR algorithm ADMIRE at strength level 3. The PC-CT images were reconstructed with the Quantum Iterative Reconstruction (QIR) algorithm and similar kernels, where the kernel strength levels were closely matched to the EID-CT. The images of both the EID-CT and PC-CT were reconstructed with a slice thickness of 1.0 mm and an increment of 0.7 mm. The standard protocol for reconstructing non-contrast images on the PC-CT scanner entails the generation of virtual monoenergetic images (VMI) at 70 keV through spectral analysis.

Sixteen alternative reconstructions were acquired of the baseline scan protocol of the Catphan and Lungman phantoms, with only one parameter altered at a time relative to baseline, namely: (*i*) VMIs at 60, 65, 80 and 90 keV, (*ii*) QIR level 1, 2, and 4, (*iii*) slice thickness/increment of 0.8/0.7, 0.6/0.5 and 0.4/0.2 mm, and (*iv*) kernels Br36, Br44, Bl60, Bl64, Qr76, Qr89. Table 2.2 provides an overview of the presented information.

2.4. PULMONARY NODULE DETECTION

One experienced reader, with extensive expertise in analyzing over 11.000 pulmonary chest CT examinations, performed the nodule detection of the Lungman images obtained at different dose levels. A second reader will evaluate the images at a later stage. The images were evaluated in four separate batches, each consisting of 30 CT scans, in Syngo.Via (Siemens Healthcare GmbH, Erlangen, Germany) and in a random order, such that three consecutive scans featured a distinct nodule setup. The Br kernel was dedicated for the nodule detection, using the maximum intensity projection (MIP) at 10 mm slice thickness. The Bl kernel was also available for additional information with a window level (W/L) setting of approximately W = 1200 HU and L = -600 HU and was only subject to additional adjustments of the reader's preference. All the findings were compared with the recorded nodule locations and the 100% dose CT to confirm the presence of a nodule. The volume measurements were performed on the Bl/Qr kernel images in a later stage of the study.

After all images were evaluated, the sensitivity and precision were computed using the following equations:

$$Sensitivity = \frac{TP}{TP + FN} \tag{2.1}$$

$$Precision = \frac{TP}{TP + FP} \tag{2.2}$$

where TP represents the true positive nodules, FN represents false negative nodules (*i.e.*, present but not detected), and FP represents the false positive nodules. The determination of specificity for nodules specifically was not possible due to the absence of TN nodules. Consequently, all scans were categorized as TN except if a FP finding was present, not considering the TP nodules present in the images used for sensitivity analysis. The specificity was computed using the following equation:

$$Specificity = \frac{TN}{TN + FP^{img}} \tag{2.3}$$

where TN represents the number of images without FP findings, and FP^{img} represents the number of images with one or more FP finding. In addition, the total number of FP findings was recorded.

2.5. IMAGE QUALITY EVALUATION

The software *iQMetrix-CT* is developed for a task-based image quality assessment by computing the metrics NPS, TTF and detectability index (d'). Several publications [26–29] have cited the well-known methodology utilized by this software [30]. The images of the Catphan PC-CT and the reference EID-CT were automatically analysed with the *iQMetrix-CT* software, the homogeneous module (CTP486) for NPS calculation and the module containing cylindrical inserts (CTP404) for TTF calculation.

2.5.1. NOISE POWER SPECTRUM

The NPS measures the magnitude of image noise as well as the spatial correlation of noise properties, *i.e.* noise texture, as described in detail by Samei et al. [31]. Lower peak frequencies

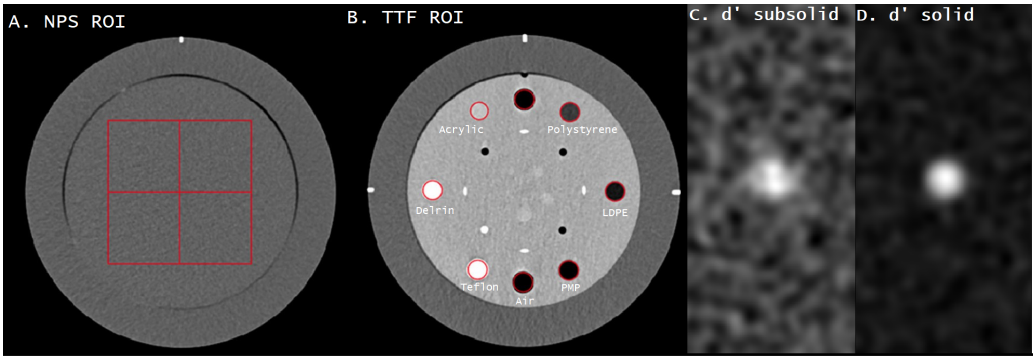

Figure 2.4: Catphan 600 phantom with regions of interest (ROIs) for the noise power spectrum (NPS) in the homogeneous module (CTP486) (A), and the sensitometry samples in the CTP404 module for the task-based transfer function (TTF) (B). For the detectability index (d') both the NPS and TTF are combined in a task function of a 5 mm subsolid nodule (C) using the Delrin insert, and a 4 mm solid nodule (D) using the Teflon insert.

correspond to a grainier texture, whereas high spatial frequency of the peak corresponds to a fine texture [27]. In each slice of the homogeneous section, four regions of interest (ROIs) were placed in the center. The size of each square ROI varied depending on the image's matrix size, with 78, 116, and 156 pixels per square side for images with 512, 768, and 1024 matrix size, respectively (figure 2.4). Hereafter, the 2D NPS profiles were obtained in the axial plane and then averaged to generate the 1D NPS curve. The raw NPS data was fitted with a smoothing spline-type filter within the iQMetrix-CT software [30]. The coefficient of determination (R^2) was then calculated using Microsoft Excel (version 2208), providing a quantitative assessment of the goodness-of-fit of the NPS curves to the raw data (figure 2.5). The noise magnitude (area under the curve), NPS_{peak} and f_{peak} were extracted.

2.5.2. TASK-BASED TRANSFER FUNCTION

The axial contrast-dependent spatial resolution was computed with the TTF, as described in detail by Greffier et al. [30] and Samei et al. [31]. The ROIs were automatically placed around the detected Teflon and Delrin inserts or manually selected if missing (figure 2.4). The pixel HU values versus the distance from the center in the ROIs make up the edge spread function (ESF). The line spread function is the derivative of the smooth ESF, fitted with a sigmoid and two gaussians, whereafter it is Fourier transformed to obtain the TTF. The R^2 value was subsequently computed to quantitatively evaluate the goodness-of-fit of the ESF curves to the raw data (figure 2.5). Due to the requirement of repeating the calculations to obtain the raw ESF data, the R^2 was computed exclusively for the three standard reconstruction kernels of

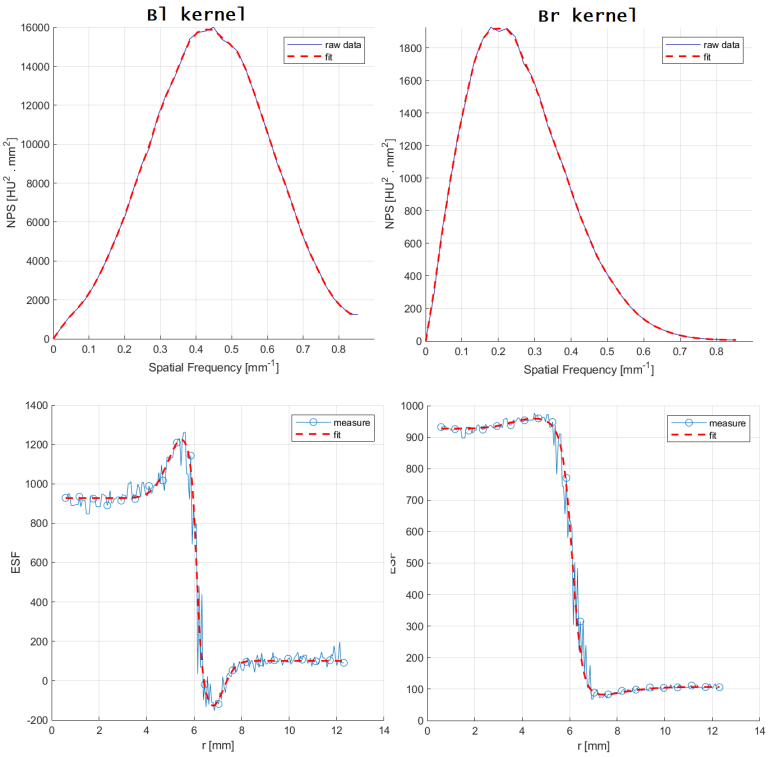

Figure 2.5: Example (top row) of the raw NPS data fitted with a smoothing spline-type filter within the iQMetrix-CT software. On the second row an example of the edge-spread fucntion (ESF) fitted with a sigmoid and two gaussians, used to calculate the task-based transfer function (TTF) with iQMetrix-CT. Both examples display the Bl and Br kernel.

both CT systems, as well as for scans exhibiting atypical TTF curves. As the spatial frequency increases (i.e. line spacing decreases), it becomes increasingly difficult for the detector and image reconstruction algorithm to efficiently transfer this information. The TTF value at 50% was extracted ($TTF_{50\%}$) to represent the spatial resolution.

2.5.3. DETECTABILITY INDEX

To account for and quantify the combined effects of contrast, noise, and spatial resolution on the image quality the detectability index (d') was computed using a non-pre-whitening with eye filter and internal noise (NPWEi) model observer, proposed by Saunders et al. [32]. An increase in d' implies the signal is easier to detect and thus image quality is better [31]. The properties of the clinical task were set to simulate a circular pulmonary nodule of 4 mm (solid) and 5 mm (subsolid) using the TTF results of the Teflon and Delrin inserts, respectively (figure 2.4). These sizes correspond to the positive nodule thresholds similar to those used in the NLST [7, 33]. Interpretation conditions for the d' calculations were set to a viewing distance of 500 mm, 0.2 mm pixel display, 3280 x 2048 pixel matrix of the display screen and zoom factor of 1.5, similar to previous studies [26, 28, 31].

2.5.4. STATISTICAL ANALYSIS

The performance of radiologists in detecting nodules for each dose level of the PC-CT and reference EID-CT protocols was quantified by the calculation of the sensitivity, specificity and related 95% CI, using the Wilson score interval [34]:

$$\frac{\left(2n\hat{p} + z_{1-\alpha/2}^2\right) \pm z_{1-\alpha/2}\sqrt{z_{1-\alpha/2}^2 + 4n\hat{p}(1-\hat{p})}}{2\left(n + z_{1-\alpha/2}^2\right)} \tag{2.4}$$

where $\hat{p}$ is the population sensitivity/specificity, n represents the total number of nodules/images and $z = 1.96$. This was done for each nodule's size, shape, and density. The results were reported as mean or, when possible, as mean ± standard deviation (SD).

3
RESULTS

3.1. PULMONARY NODULE DETECTION

The sensitivity, specificity, precision and FP findings are presented in table 3.1 of both the EID-CT and the PC-CT. The full table can be found in Appendix B.2, and specifically for the different nodule shape and densities in Appendix B.1. The experienced reader achieved a sensitivity of 58%, 59%, 62%, 55% and 51% at 100%, 75%, 50%, 25% and 10% dose on the PC-CT, respectively, and a 59% sensitivity on the EID-CT. No significant difference in sensitivity was found between the different CT scanners and dose levels, since the 95% confidence interval (CI) all overlap (figure 3.1). The EID-CT and PC-CT both demonstrated high specificity of 100% and 95%, respectively. However, the specificity decreased to 90%, 80%, 75% and 50% when the dose on the PC-CT was lowered to 75%, 50%, 25% and 10%, which was significantly lower than the EID-CT at 100% dose. Both PC-CT and EID-CT achieved a precision of 99% and 100% at the reference dose, respectively. However, the precision of PC-CT decreased as the dose decreased. Specifically, at a dose of 10%, PC-CT resulted in 15 FP nodules, whereas the number of FP nodules for EID-CT and the other PC-CT dose levels were all less than or equal to 5. Figure 3.3 illustrates the changes in image quality across various dose levels for both PC-CT and EID-CT scans of the right lung.

Figure 3.2 and table 3.2 display the sensitivity for each nodule size. For nodules that were 5 mm or larger, the sensitivity was at least 89%, except for the PC-CT at the 10% dose level, where it was 72%. In contrast, for nodules smaller than 5 mm, the sensitivity dropped to 39-61% for the 4 mm nodule, and to 22% or lower for nodules of 3 mm and below. The sensitivity for nodules ranging from 3-5 mm in diameter is shown to be more strongly influenced by the dose level, as depicted by the larger range in sensitivity in figure 3.2. In contrast, the larger nodules (>5 mm) consistently achieved high sensitivity levels, while the 2.5 mm nodules were generally not detected.

Table 3.1: The sensitivity, specificity, precision and false positive (FP) nodules of the EID-CT and PC-CT at 100% dose (0.8 mGy), and for decreasing dose levels (0.61 mGy (75%), 0.41 mGy (50%), 0.20 mGy (25%) and 0.07 mGy (10%)), are presented overall. *Specificity was determined by calculating the true negatives (TN) and FP per image.

Reader 1 (GJ)	Sensitivity (95% CI)	Specificity* (95% CI)	Precision	FP
EID	59% (49-68%)	100% (97-100%)	100%	0
PC 100%	58% (48-67%)	95% (89-98%)	99%	1
PC 75%	59% (49-68%)	90% (83-94%)	97%	3
PC 50%	62% (52-70%)	80% (71-86%)	97%	3
PC 25%	55% (46-64%)	75% (66-82%)	94%	5
PC 10%	51% (42-61%)	50% (41-59%)	88%	15

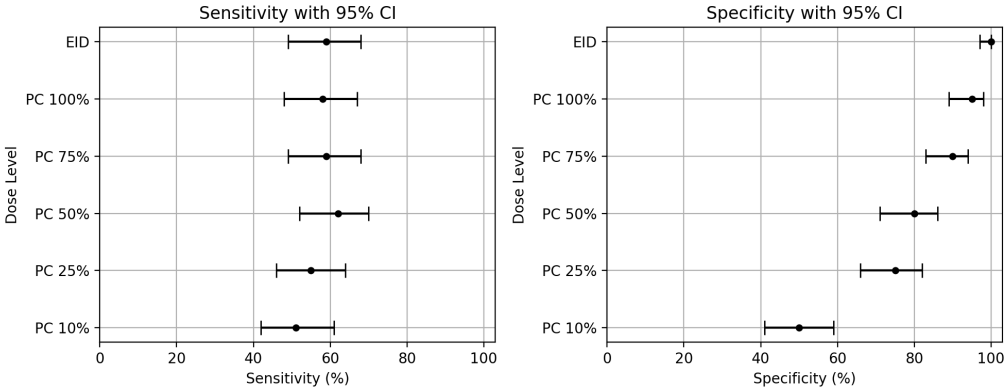

Figure 3.1: Sensitivity and specificity with 95% CI for the detection of artificial pulmonary nodules for EID-CT and PC-CT at 100% dose (0.8 mGy), and for decreasing dose levels (0.61 mGy (75%), 0.41 mGy (50%), 0.20 mGy (25%) and 0.07 mGy (10%)).

Table 3.2: The sensitivity of the EID-CT and PC-CT at 100% dose (0.8 mGy), and for decreasing dose levels (0.61 mGy (75%), 0.41 mGy (50%), 0.20 mGy (25%) and 0.07 mGy (10%)), are presented for every nodule diameter (⌀)

Nodule ⌀ [mm]	2.5	3	4	5	6	10
EID	0% (0/18)	22% (4/18)	50% (9/18)	89% (16/18)	94% (16/17)	100% (18/18)
PC 100%	6% (1/18)	11% (2/18)	39% (7/18)	94% (17/18)	100% (17/17)	100% (18/18)
PC 75%	0% (0/18)	17% (3/18)	56% (10/18)	89% (16/18)	94% (16/17)	100% (18/18)
PC 50%	6% (1/18)	11% (2/18)	61% (11/18)	94% (17/18)	100% (17/17)	100% (18/18)
PC 25%	6% (1/18)	0% (0/18)	39% (7/18)	89% (16/18)	100% (17/17)	100% (18/18)
PC 10%	0% (0/18)	6% (1/18)	39% (7/18)	72% (13/18)	100% (17/17)	94% (17/18)

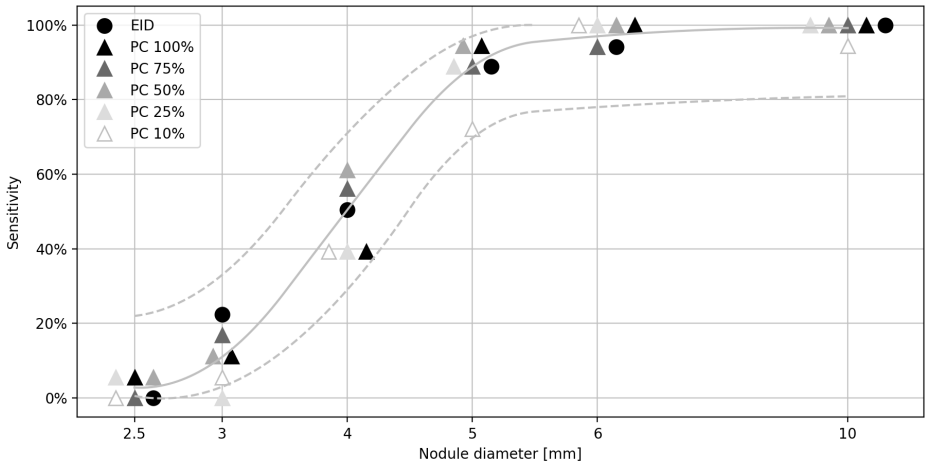

Figure 3.2: Sensitivity (CI 95%) of the detection of artificial pulmonary nodules for EID-CT and PC-CT at 100% dose (0.8 mGy), and for decreasing dose levels (0.61 mGy (75%), 0.41 mGy (50%), 0.20 mGy (25%) and 0.07 mGy (10%)).

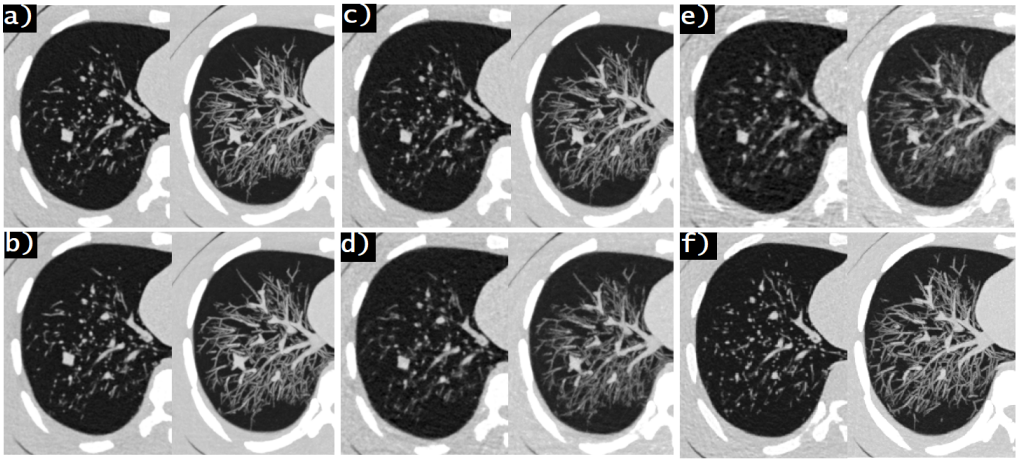

Figure 3.3: Right lung of the Lungman phantom scanned with the PC-CT at 0.81 mGy (a, 100%), 0.61 mGy (b, 75%), 0.41 mGy (c, 50%), 0.20 mGy (d, 25%) and 0.07 mGy (e, 10%), and with the EID-CT at 0.79 mGy (f). Right) Br kernel in axial view, Left) Br kernel maximum intensity projection (MIP) at 10 mm slice thickness. Image (f) is of the EID-CT with a different nodule setup and therefore does not contain the nodule seen in the other images.

3.2. IMAGE QUALITY EVALUATION

The results of the NPS, TTF and d' are described below, and a full overview can be found in table 3.3. Figure 3.4 illustrates the differences in image quality resulting from variations in IR level, VMI level, and scan modes for both PC-CT and EID-CT.

3.2.1. NOISE POWER SPECTRUM

NPS curves obtained of all Catphan images are depicted in figure 3.5 and the values for noise (magnitude and NPS_{peak}) and noise texture (f_{peak}) are given in table 3.3. All the curves had an R^2 value greater than 0.99, indicating a strong fit between the fitted curves and the raw data from the iQMetrix-CT software. The NPS spatial frequency data refers to the frequency at which the maximum of the NPS is reached. Higher spatial frequencies imply finer noise texture, whereas lower frequencies indicate coarser or grainier texture [27].

The PC-CT noise magnitude was 29% lower than the conventional EID-CT, both using the standard-of-care lung cancer screening CT protocol with tin filter, and utilizing similar dose levels and reconstruction methods. However, the noise texture was relatively similar, with a slight shift to the lower-end for the PC-CT. The noise magnitude decreased with a higher QIR level, as well as the f_{peak}. Between QIR1 and QIR4 the noise magnitude and f_{peak} decreased with 44% and 33%, respectively. Interestingly, the NPS curves of QIR1 and ADMIRE3 were very similar. The noise magnitude decreased with a higher VMI energy level, although the f_{peak} at 70 keV was positioned most to the right, indicating a finer noise texture. The f_{peak} remained constant with a varying slice thickness and increment, although substantial reductions in noise magnitude were found (*e.g.* -35% between 0.4/0.2 mm and 1.0/0.7 mm). The results show that the EID-CT had an overall higher noise magnitude when looking at the different kernels; *i.e.* 40% Br40, 69% Bl56/57 and 43% Qr60/59 increase compared to the PC-CT. An increase in kernel sharpness on the PC-CT was linked to an increase in noise as well as an increase in the f_{peak}, suggesting a trade-off between noise texture and magnitude. The UHR scan modes

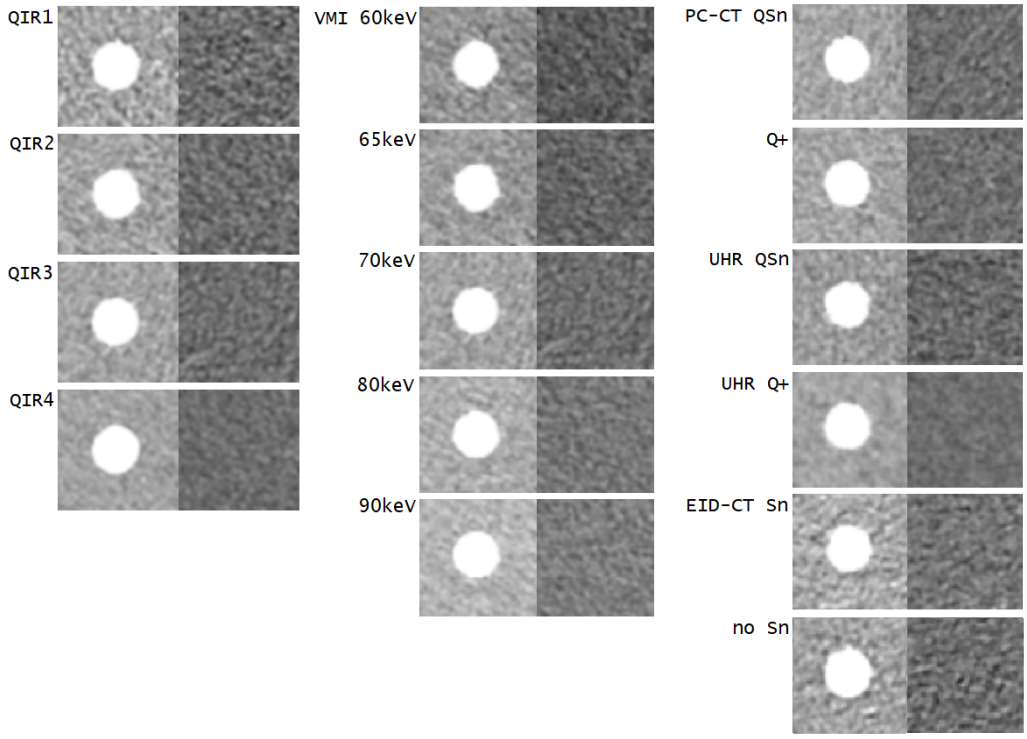

Figure 3.4: *Different levels of IR, VMI keV and scan modes on image quality in PC-CT and EID-CT. The Delrin insert (left) and homogeneous area (right) were used for calculating TTF and NPS, respectively. Images of Br kernel with W/L-settings: W 400, L 40.*
(QIR, quantum iterative reconstruction; VMI, virtual monoenergetic image; UHR, ultra-high resolution; QSn, 100kV with tin filter; Q+, 120kV no filter)

showed similar patterns, where Br40 had the least noise and Bl56 had more noise than the Qr56 kernel in both the Q+ and QSn scan mode. Qr89 showed a 356% (QSn) and 667% (Q+) noise increase compared to Qr60, but also had a lower slice thickness (0.2 *vs.* 0.4 mm). The presence or absence of a tin filter did not make a difference in the magnitude of noise for both CT scanners, except in the UHR scan modes where noise magnitude and f_{peak} increased with tin filter. Overall, the UHR Q+ mode achieved the lowest level of noise, but also the lowest f_{peak}.

3.2.2. TASK-BASED TRANSFER FUNCTION

The TTF curves obtained for the Delrin (subsolid; low contrast) and Teflon (solid; high contrast) inserts are depicted in figure 3.6 and 3.7, and the $TTF_{50\%}$ are reported in table 3.3. All the curves that were evaluated for goodness-of-fit had an R^2 value greater than 0.95, indicating a good fit between the fitted curves and the raw ESF data from the iQMetrix-CT software (Appendix C).

For both inserts, the TTF curves were relatively constant with increasing IR level on the PC-CT. QIR4 showed a small increase compared to QIR1-3, similar to ADMIRE3 on the EID-CT. Likewise, VMI energy level and slice thickness did not seem to have a substantial effect on the spatial resolution. The TTF curves shifted towards higher spatial frequencies when increas-

ing the Br kernel resolution level. This effect was most evident for the high-contrast insert, where the Br44 kernel increased the $TTF_{50\%}$ by 40% compared to the Br36 kernel. Similarly, the $TTF_{50\%}$ of the Bl56 kernel was the lowest with respect to the higher kernel levels. However, it is worth noting that the measurements displayed a considerable amount of variation for the Delrin insert (shaded area, figure 3.7). Furthermore, when the Bl kernels were used, the TTF demonstrated a substantial overshoot above unity on the high-contrast insert. This overshoot appeared as a noticeable 'halo' around the insert, depicted in figure 3.8, while it was absent when the Qr kernels were employed. Interestingly, the Qr kernels showed no right-shift of the TTF curves corresponding to the kernel resolution level. A comparison of the kernels between the PC-CT and EID-CT showed relatively similar TTF curves, although the EID-CT provided the highest $TTF_{50\%}$ for the low-contrast insert overall. When comparing the four scan modes on the PC-CT at a similar dose level and reconstruction kernel, the Q+ and QSn achieved slightly higher $TTF_{50\%}$ values compared to the UHR QSn and UHR Q+ mode. The EID-CT had a similar level of resolution overall, except for the 42% increase compared to the PC-CT with tin filter (Sn *vs.* QSn) for the high-contrast insert. In UHR mode the spatial resolution of the low-contrast insert remained largely unaffected by different kernels and strength levels, except for the Bl56 kernel, which showed a substantial increase of 82% (UHR Q+) and 64% (UHR QSn) compared to the Qr56 kernel. The TTF curves for the high-contrast insert showed a similar behavior, where the Bl56 kernel increased the $TTF_{50\%}$ by 274% (UHR Q+) and 183% (UHR QSn) compared to Qr56. Moreover, similar to the QSn mode, the Qr kernels showed no right-shift of the TTF curves corresponding to the kernel resolution level.

3.2.3. DETECTABILITY INDEX

Figure 3.9 and table 3.3 depict the d' values obtained with varying acquisition and reconstruction settings. Table 3.3 also provides an overview of the contrast values used for the d' calculation. On the PC-CT, the mean contrast values were 264 ± 3 HU for the Delrin insert and 880 ± 15 HU for the Teflon insert. For all scan modes and reconstruction settings using the Br40 kernel, the contrast values of the Delrin (low contrast) insert were comparable. However, the contrast of the Teflon insert decreased with higher VMI energy levels and tin filter application. In addition, the contrast of both inserts varied depending on the type of reconstruction kernel.

The d' values for both the low-contrast and high-contrast insert showed an increase with each subsequent IR level. The VMI energy levels had a minimal impact on the d' values, where 70 keV and 90 keV marginally provided the highest d' for the low and high-contrast insert, respectively. Regarding slice thickness, the 1.0/0.7 mm setting demonstrated a two-fold increase in d' compared to the 0.4/0.2 mm slice thickness. The three kernel types demonstrated higher d' values at the lowest strength levels, *i.e.* Br36, Bl56 and Qr60. Among the UHR scan modes, similar patterns were observed. Notably, Qr56 generally outperformed Bl56, particularly in the UHR Q+ mode for the high-contrast insert. In comparison to the EID-CT, the PC-CT attained higher d' values across all scan modes. Specifically, the d' values were 30% and 40% higher for low and high-contrast, respectively, than those of the EID-CT without a tin filter. Similarly, when a tin filter was used, the d' values were 40% and 50% higher with the PC-CT for low and high-contrast, respectively. The highest d' values were observed in the UHR Q+ mode on the PC-CT, followed by the Q+ mode for the high-contrast insert and the QSn mode for the low-contrast insert.

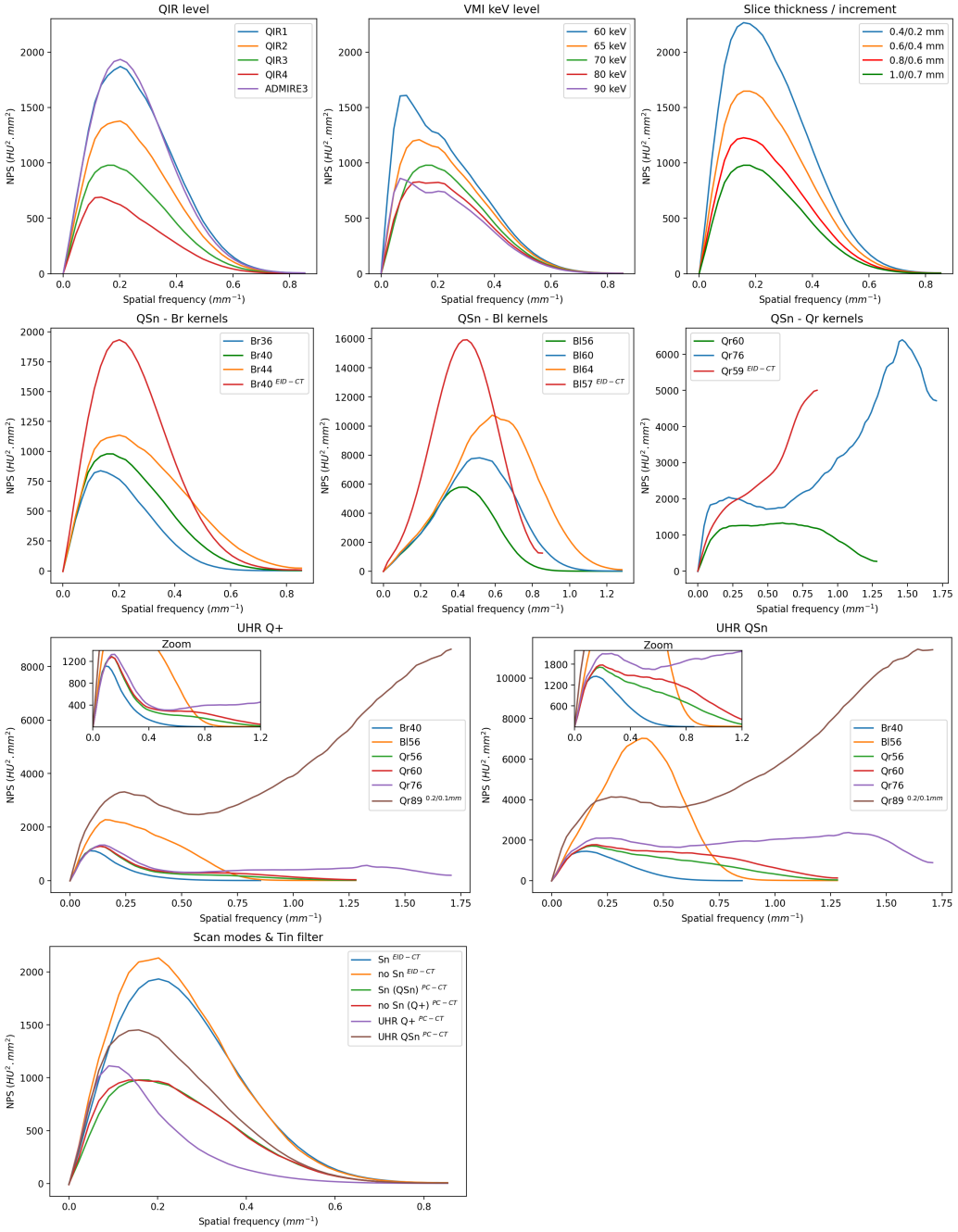

Figure 3.5: Noise Power Spectrum (NPS) curves obtained at varying acquisition and reconstruction settings. IR, iterative reconstruction; ADMIRE, IR on EID-CT; QIR, Quantum IR; VMI, Virtual Monoenergetic Images; Br, Body regular kernel; Bl, Lung kernel; Qr, Quantitative kernel; UHR, Ultra-High Resolution; Q+, Quantum plus mode (120 kV); QSn, Quantum mode (100 kV) with tin filter.

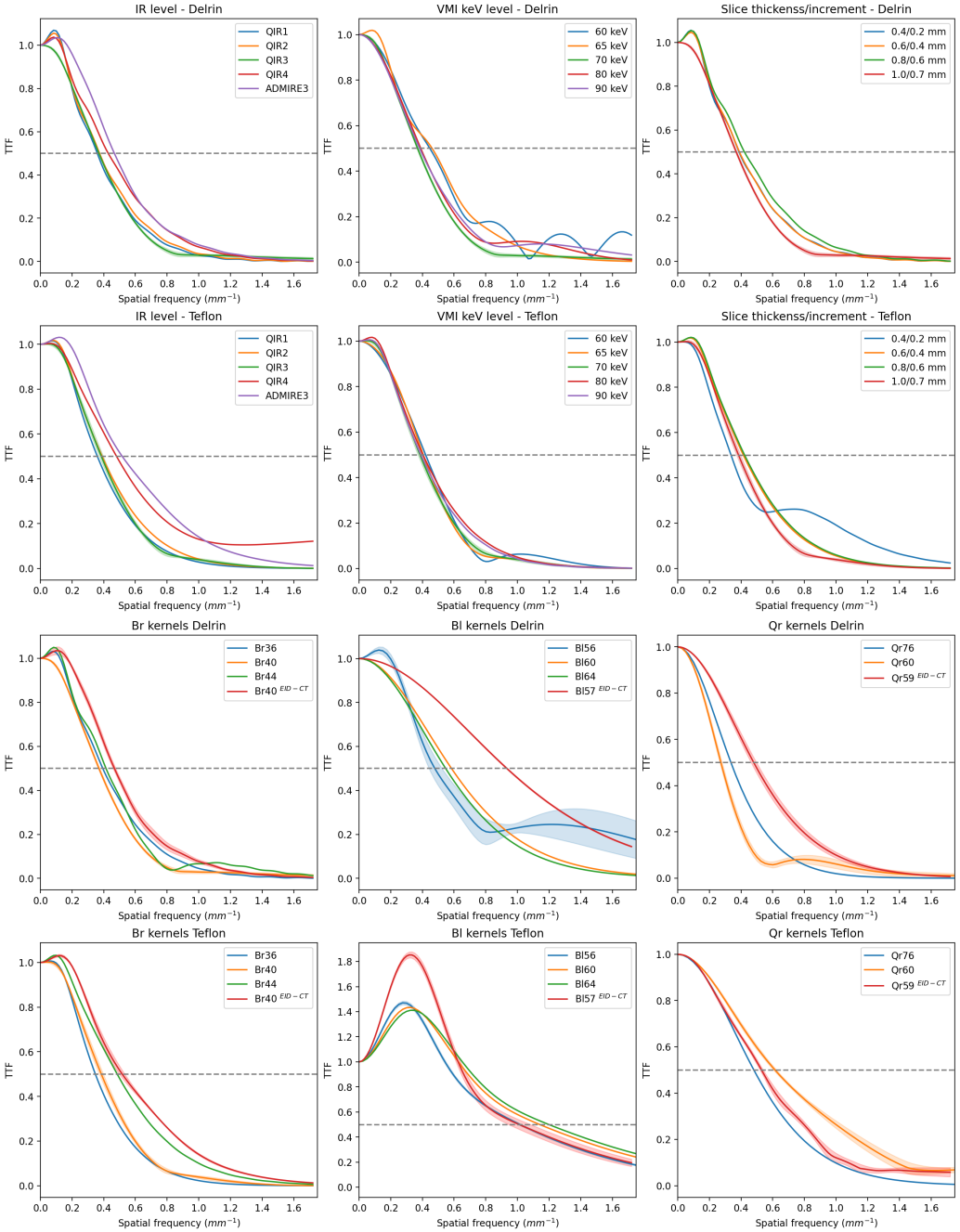

Figure 3.6: Task-based Transfer Function (TTF) curves obtained at varying acquisition and reconstruction settings of the Teflon (high contrast) and Delrin (low contrast) inserts. Standard errors are shown as a shaded area around the curve. Standard errors are reported as colored areas. IR, iterative reconstruction; ADMIRE, IR on EID-CT; QIR, Quantum IR; VMI, Virtual Monoenergetic Images; Br, Body regular kernel; Bl, Lung kernel; Qr, Quantitative kernel; UHR, Ultra-High Resolution; Q+, Quantum plus mode (120 kV); QSn, Quantum mode (100 kV) with tin filter.

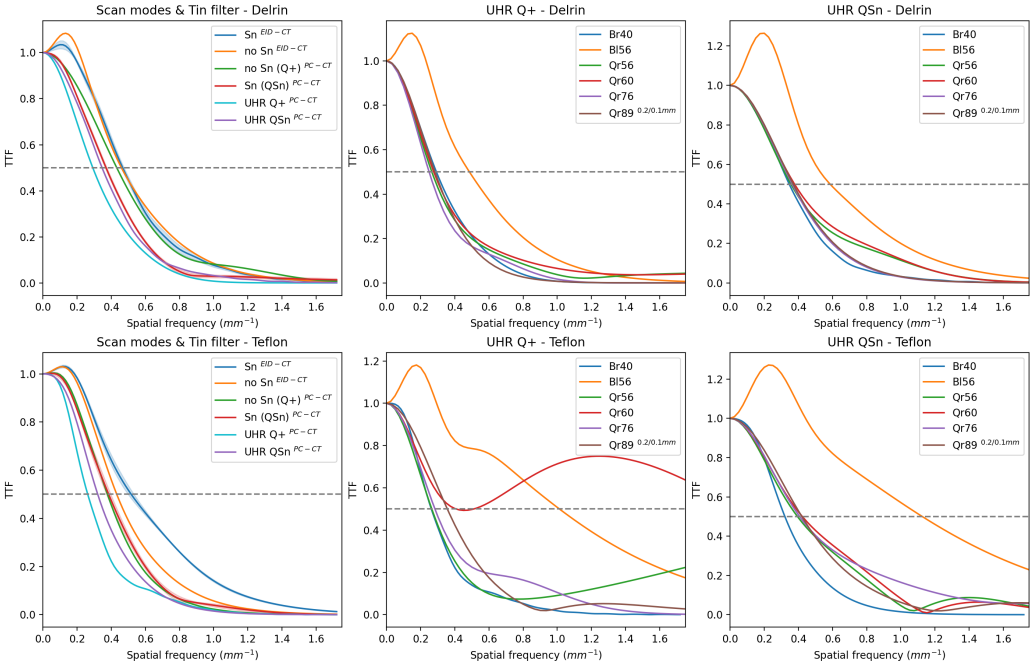

Figure 3.7: Task-based Transfer Function (TTF) curves obtained at varying acquisition and reconstruction settings of the Teflon (high contrast) and Delrin (low contrast) inserts. The Scan modes & Tin filter TTFs are of the Br40 kernel. Standard errors are reported as colored areas. IR, iterative reconstruction; ADMIRE, IR on EID-CT; QIR, Quantum IR; VMI, Virtual Mono-energetic Images; Br, Body regular kernel; Bl, Lung kernel; Qr, Quantitative kernel; UHR, Ultra-High Resolution; Q+, Quantum plus mode (120 kV); QSn, Quantum mode (100 kV) with tin filter.

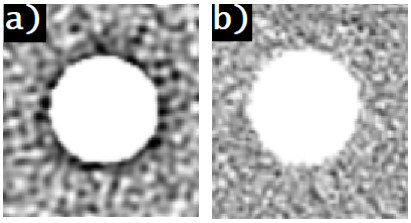

Figure 3.8: The overshoot in the task-based transfer function (TTF) due to an increase in contrast of image details can be observed as a 'halo' around the Teflon insert with the Bl56 kernel (a), whereas the Qr60 kernel (b) shows contrast increas and no overshoot in the TTF curve.

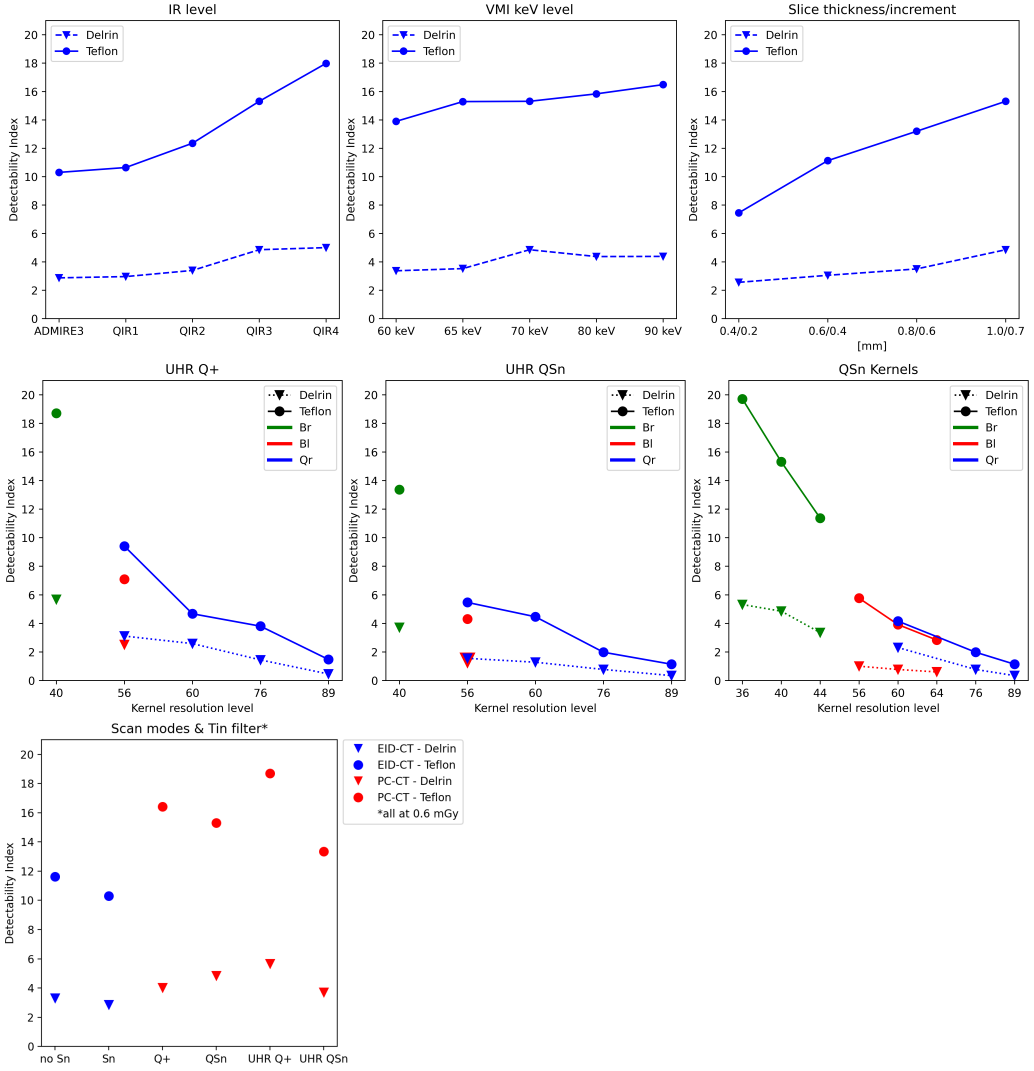

Figure 3.9: Detectability index (d') of different acquisition and reconstruction settings for the detection of solid (Teflon; 4 mm, 850 HU contrast) and subsolid (Delrin; 5mm, 275 HU contrast) simulated pulmonary nodules. All scans had a $CTDI_{vol}$ of 0.55/0.56 mGy. IR, iterative reconstruction; ADMIRE, IR on EID-CT; QIR, Quantum IR; VMI, Virtual Monoenergetic Images; Br, Body regular kernel; Bl, Lung kernel; Qr, Quantitative kernel; UHR, Ultra-High Resolution; Q+, Quantum plus mode (120 kV); QSn, Quantum mode (100 kV) with tin filter.

Table 3.3: Task-based image quality assessment results of the noise power spectrum (NPS), task-based transfer function (TTF) and detectability index (d').

		NPS			TTF		Detectability			
	Parameter	**Noise [HU]**	**NPS peak [HU^2 .mm^2]**	**F_{peak} [mm^{-1}]**	**$TTF_{50\%}$**		**d'**		**Contrast [HU]**	***
					Delrin	***Teflon***	***Delrin***	***Teflon***	***Delrin***	***Teflon***
PC-CT										
QIR	*1*	32.82	1869.69	0.20	0.359	0.360	2.960	10.643	262	873
	2	27.94	1377.75	0.20	0.373	0.390	3.394	12.355	263	873
	3 **	23.12 ± 0.06	982.86 ± 8.34	0.18 ± 0.02	0.37 ± 0.01	0.42 ± 0.02	4.38 ± 0.24	15.28 ± 0.5	262 ± 1	873 ± 1
	4	18.27	690.62	0.14	0.428	0.481	5.001	17.979	263	874
VMI	*60 keV*	26.74	1608.84	0.09	0.447	0.420	3.368	13.894	260	889
	65 keV	25.14	1209.42	0.14	0.461	0.406	3.523	15.288	261	880
	70 keV **	23.12 ± 0.06	982.86 ± 8.34	0.18 ± 0.02	0.36 ± 0.02	0.42 ± 0.02	4.38 ± 0.24	15.28 ± 0.5	262 ± 1	873 ± 1
	80 keV	21.73	828.69	0.14	0.390	0.404	4.371	15.833	265	864
	90 keV	20.94	860.60	0.07	0.383	0.391	4.382	16.482	266	857
Slth/incr [mm]	*1,0/0,7* **	23.12 ± 0.06	982.86 ± 8.34	0.18 ± 0.02	0.36 ± 0.02	0.42 ± 0.02	4.38 ± 0.24	15.28 ± 0.5	262 ± 1	873 ± 1
	0,8/0,6	35.74	2265.19	0.16	0.387	0.337	3.500	13.199	263	873
	0,6/0,4	30.57	1647.31	0.16	0.390	0.415	3.050	11.127	262	872
	0,4/0,2	25.96	1226.69	0.16	0.421	0.423	2.555	7.448	263	874
Kernels	*Br36*	17.97	837.90	0.14	0.394	0.347	5.315	19.704	266	885
	Br40 **	23.12 ± 0.06	982.86 ± 8.34	0.18 ± 0.02	0.36 ± 0.02	0.42 ± 0.02	4.38 ± 0.24	15.28 ± 0.5	262 ± 1	873 ± 1
	Br44	29.56	1135.32	0.20	0.428	0.481	3.351	11.363	261	867
	Bl56 *	81.87 ± 0.1	5819.52 ± 29.02	0.42 ± 0.02	0.50 ± 0.1	1.02 ± 0.02	1.14 ± 0.1	5.59 ± 0.14	279 ± 3	901 ± 2
	Bl60	112.25	7808.19	0.52	0.58	1.14	0.77	3.92	275	897
	Bl64	151.07	10740.81	0.58	0.55	1.20	0.60	2.83	271	894
	Qr60 *	69.95 ± 0.06	1352.27 ± 14.56	0.61 ± 0.04	0.27 ± 0.02	0.61 ± 0.02	1.7 ± 0.38	4.11 ± 0.2	248 ± 2	827 ± 2
	Qr76	199.57	6400.64	1.46	0.34	0.48	0.55	1.72	247	830
Q+	*Br40*	23.13	978.32	0.14	0.43	0.38	4.04	16.43	263	896
	Bl56	82.84	5772.75	0.43	0.32	1.15	0.57	4.89	285	926
	Qr60	71.66	1415.01	0.65	0.23	0.45	2.35	4.27	251	848
UHR QSn	*Br40*	26.24	1452.07	0.16	0.35	0.32	3.71	13.36	267	904
	Bl56	88.43	7025.75	0.40	0.59	1.13	1.42	4.31	281	937
	Qr56	55.13	1716.79	0.18	0.36	0.40	1.55	5.47	253	854
	Qr60	66.98	1778.73	0.20	0.38	0.42	1.28	4.46	253	856
	Qr76	133.35	2379.63	1.33	0.36	0.41	0.77	1.98	250	858
	Qr89	305.70	11422.52	1.64	0.37	0.42	0.34	1.14	245	823
UHR Q+	*Br40*	16.53	1112.22	0.09	0.29	0.26	5.68	18.71	272	912
	Bl56	45.78	2274.93	0.16	0.49	1.01	2.51	7.09	286	946
	Qr56	29.02	1285.61	0.14	0.27	0.27	3.11	9.40	258	860
	Qr60	33.95	1280.59	0.14	0.28	0.41	2.58	4.67	257	861
	Qr76	62.64	1326.90	0.16	0.25	0.28	1.44	3.80	255	863
	Qr89	260.84	8650.45	1.71	0.28	0.36	0.46	1.47	248	842
EID-CT *										
Sn	*Br40*	32.47 ± 0.07	1934.09 ± 16.31	0.20 ± 0	0.47 ± 0.02	0.51 ± 0.04	3.13 ± 0.16	10.23 ± 0.18	257 ± 1	841 ± 3
	Bl57	138.34 ± 0.11	15852.17 ± 60.99	0.45 ± 0	0.70 ± 0.04	1.04 ± 0.13	0.99 ± 0.06	4.21 ± 0.06	258 ± 1	844 ± 3
	Qr59	99.97 ± 0.11	5190.47 ± 120.30	0.84 ± 0.01	0.53 ± 0.04	0.53 ± 0.02	0.78 ± 0.07	3.02 ± 0.12	240 ± 1	790 ± 3
no Sn	*Br40*	33.03	2132.39	0.20	0.46	0.43	3.31	11.616	263	876
	Bl57	136.17	16037.13	0.45	0.95	1.04	0.589	4.389	264	879
	Qr59	96.05	4498.34	0.85	0.44	0.52	1.006	3.179	246	821

* Acquisition was repeated five times, to assess the error in d' values, and are therefore depicted as mean ± SD

** Standard settings, used in previous lung cancer screening protocols.

*** Contrast defined as the difference in attenuation between insert and surrounding material.

EID-CT, Energy-integrating detector Computed Tomography; PC-CT, Photon-Counting CT; NPS, Noise Power Spectrum; TTF, Task-based Transfer Function; d', detectability index; Slth/incr, slice thickness / increment; IR, iterative reconstruction; ADMIRE, IR on EID-CT; QIR, Quantum Iterative Reconstruction; VMI, Virtual Monoenergetic Images; Br, Body regular kernel; Bl, Lung kernel; Qr, Quantitative kernel; UHR, Ultra-High Resolution; Q+, Quantum plus mode (120 kV); QSn, Quantum mode (100 kV) with tin filter.

4

DISCUSSION

The findings of this phantom study showed that low-dose lung cancer screening using PC-CT is feasible and offers comparable diagnostic accuracy to conventional EID-CT. At a dose of 10%, the PC-CT demonstrated no significant difference in sensitivity to the EID-CT. However, it only achieved comparable specificity when operated at a dose of 100%. Furthermore, objective assessments of image quality revealed that PC-CT reduced noise magnitude and achieved an overall higher d' value compared to EID-CT at a similar dose, irrespective of scan mode or tin filter application. There were no major differences in spatial resolution observed between the two CT scanners, likely due to possible limitations in the iQMetrix-CT software and similar reconstruction settings employed. Several preliminary studies have shown the potential of PC-CT for lung cancer screening, offering advantages in terms of dose and spatial resolution [35–38]. However, to date, no study has comprehensively evaluated the sensitivity and specificity of PC-CT at different dose levels by human readers or performed a task-based image quality assessment of PC-CT in comparison to EID-CT, particularly in the context of low-dose lung cancer screening protocols and with a range of acquisition and reconstruction settings.

4.1. MAIN FINDINGS

4.1.1. PULMONARY NODULE DETECTION

PC-CT showed no significant difference in sensitivity overall at dose levels down to 10% of the original dose. Furthermore, this study showed that EID-CT and PC-CT at 25-100% dose are equally effective in detecting lung nodules with a diameter of 5 mm or larger with a sensitivity of 89% or higher. However, for nodules smaller than 5 mm, both CT systems exhibited reduced sensitivity. The disadvantages of ultra-low dose levels were most apparent when the dose was reduced from 25% to 10% and the specificity decreased from 75% to 50%. Moreover, the precision remained 94% or higher on the PC-CT until a dose level of 25%, but at 10% dose decreased to 88% and showed a three-fold increase in FP findings. A more comprehensive overview will be obtained after the second reader's results are available. This will facilitate a more robust and informed comparison.

In the NELSON study, sensitivity of the baseline screening for lung cancer detection was 94.6%, and specificity 98.3%, similar to the EID-CT and 100% dose PC-CT of the present study [39, 40]. Another study used the same anthropomorphic phantom and found a similar drop-off in sensitivity below 5 mm nodules with an EID-CT [41]. In addition, they reported a sensitivity of 60-80% for solid nodules and 0-20% for non-solid nodules with a diameter of 3 mm. The current study reported a similar sensitivity of 63-67% for solid nodules. However, the low-dose CT acquisition protocol reported in Xie et al. [41] did not specify the dose level, limiting the comparability of results. Previous studies have investigated ULD protocols for lung cancer

screening on EID-CT, and have demonstrated comparable diagnostic performance to LD CT protocols [42–47]. Ye et al. conducted two studies [48, 49] that investigated the feasibility of an ULD chest protocol (0.1 mGy) on EID-CT and reported a sensitivity of 98-100% for nodules ≥6 mm, which is comparable to the current finding of 94%-100% sensitivity with the PC-CT at 10% dose (0.07 mGy). However, the sensitivity analysis of ULD CT by Ye et al. [48, 49] used LD CT as the reference standard, which means that (small) nodules missed on the LD CT were not considered, and thus, the actual sensitivity of the ULD CT was presumably lower. In addition, the studies did not account for the specificity or precision with ULD EID-CT. A review on lung cancer screening programs stressed the importance of FP findings and a low specificity of a screening program, leading to unnecessary diagnostic tests and invasive procedures [16]. The specificity of LDCT from thirteen studies ranged from 26.4% to 99.7%, where all but three reported specificity greater than 75% [16, 40].

4.1.2. NOISE POWER SPECTRUM

The NPS outcomes show the impact acquisition and reconstruction settings have on the noise magnitude and texture. The standard reconstruction settings of IR level (QIR3), VMI (70 keV) and slice thickness and increment (1.0/0.7 mm) all showed low noise and fine noise texture. However, an IR level of QIR4 proved to reduce the noise an additional 21.0%, although the texture becomes 22.2% coarser. Sartoretti et al. [50] found QIR3 best for sharpness and overall image quality of the lung, although QIR4 had the lowest noise. This trade-off in image texture and noise, common to all IR algorithms, is consistent with previously published studies [27, 28, 51, 52]. The use of monoenergetic images, which are derived from low- and high-energy bin signals, offers a number of advantages, including the minimization of beam hardening artifacts [53]. Images reconstructed at low keVs exhibit a higher degree of contrast, but are often contaminated by noise and artifacts arising from high-density materials. Conversely, images reconstructed at high keVs exhibit lower contrast, yet demonstrate less noise and reduced metal and high-density material artifacts [54]. The results of this study are consistent with the observation that lower keV images exhibit higher noise levels. Nonetheless, the potential benefit of enhanced contrast agent signal is not relevant for a lung cancer screening protocol. Higher kernel strengths strongly increased noise, as they tend to increase high frequency noise, and produced a finer noise texture (right shift of f_{peak}), which is in line with previous studies [22, 55, 56]. Similar to Dunning et al. [22], the images of the PC-CT were found to have less noise in comparison with the EID-CT. Greffier et al. [29] showed that a tin filter reduced the noise magnitude for the same tube voltage and did not affect image texture. Interestingly, the noise on the PC-CT was similar with or without tin filter, whereas the EID-CT showed a slight decrease with tin filter. The UHR Q+ mode resulted in the lowest noise overall, similar to the study of Jungblut et al. [37]. As a whole, the results illustrate the noise reduction capabilities of the PC detector technology compared to EID-CT. As other studies have concluded, these properties can be leveraged for ultra-low dose lung cancer screening [22, 35, 37, 50, 57, 58].

According to Dolly et al. [59], the calculation parameters can significantly affect the NPS, particularly at spatial frequencies below 0.15 mm^{-1}. The iQMetrix-CT software employs a second-order polynomial fit to remove background noise, although Dolly et al. found that image subtraction was a more effective method. Unfortunately, the software does not allow for customization of the image background removal technique. Consequently, the NPS of the VMI energy levels was recalculated using an in-house script to assess this effect. The resulting NPS curves did not intersect the origin and exhibited an increase at low spatial frequencies, while all curves shared the same f_{peak} position (see Appendix D). Although error bars are ab-

sent, the fluctuations of the curves provide an indication of their magnitude. This variability allows for several possibilities for curve fitting. Hence, while employing a background fit in iQMetrix-CT renders the curves smoother, it does not offer a more accurate representation of the data. Thus, it is important to take the impact of the calculation parameters into account, especially at low spatial frequencies, when interpreting the NPS results.

4.1.3. TASK-BASED TRANSFER FUNCTION

The results of this study demonstrate that the $TTF_{50\%}$ was largely independent of variations in IR level, VMI keV and slice thickness. For the IR level only QIR4 resulted in an improvement in spatial resolution. In contrast, Rotzinger et al. [27] reported a decrease in spatial resolution when using a higher IR level for low-contrast inserts, especially at reduced doses. It is worth noting that an increase in slice thickness is typically associated with improved spatial resolution [60]. However, this phenomenon was not observed in the current study. The choice of kernels had a more noticeable effect on the $TTF_{50\%}$, with the Bl60 kernel demonstrating a two-fold increase in spatial resolution compared to the Qr60 kernel. The overshoot observed with the Bl kernels, but not with the Qr kernels, can be attributed to the sharpening effect of the Bl kernel, which enhances the contrast of image details [61]. This sharpening effect creates a "halo" around the insert, resulting in over- and undershoot in the ESF and ultimately leading to an overshoot in the TTF. Interestingly, certain kernels were found to be better suited for the low-contrast insert (*e.g.*, Bl56/Qr76), while others were better suited for the high-contrast insert (*e.g.*, Bl64/Qr60). Overall, the change in kernel strength had a minimal impact on spatial resolution. It is worth noting that the numbering of the kernel strength corresponds to the 50% modulation transfer function (MTF) specified by the system manufacturer. For instance, Qr59 has a lower 50%-MTF than Qr60, although it can yield higher values for lower MTF percentages, potentially leading to better spatial resolution and performance (Appendix E.1). Thus, a higher kernel strength does not automatically indicate better performance. In line with this, it was expected that higher kernel levels would result in higher $TTF_{50\%}$ values. While this was marginally observed for the Br and Bl kernels, it was not evident for the Qr kernels.

In comparison to PC-CT, the EID-CT often exhibited higher spatial resolution. However, with the availability of sharper kernels the PC-CT has the potential for much higher spatial resolution. The observed similarity in resolution between PC-CT and EID-CT images is possibly a result of the similar reconstruction settings rather than a limitation of the technique itself. Moreover, contrary to expectations, the UHR scan modes did not demonstrate an increase in spatial resolution compared to other scan modes in both PC-CT and EID-CT. This finding is contradictory to previous reports that highlighted the significant increase in spatial resolution achieved by the UHR mode in PC-CT, by dividing each "macro" detector pixel into smaller sub-pixels [18]. Especially the highest kernel strength (Qr89) and smallest slice thickness (0.2 mm) combination was expected to increase spatial resolution. Multiple studies have reported improved spatial resolution with PC-CT, particularly in UHR mode, in clinical lung images [18, 22, 27, 62, 63].

Given the unexpected results obtained in TTF measurements, it is advised to exercise caution when interpreting these findings regarding spatial resolution. One possible explanation for the discrepancies could be a limitation within the iQMetrix-CT software, where the accuracy of the ESF fitting, similar to the NPS, is constrained. Although the R^2 values of the selected ESF curves indicate a good overall fit, the region where the HU transition starts and ends, *i.e.* where the edge starts and ends, is the most critical area. This region contains the information on how

well the contrast is transferred by the system. In the event of a slight misfit in this section, the data essential for accurate determination of the TTF is compromised (example in Appendix C.1). Instead of accurately representing the true TTF of the scanner and reconstruction parameters, it may reflect the limitations of the model itself. Nevertheless, the volumetry results will provide supplementary information on the spatial resolution of different reconstruction settings, as higher spatial resolution will yield smaller volumetry errors.

4.1.4. DETECTABILITY INDEX

The combined variations of noise (magnitude and texture), $TTF_{50\%}$ and contrast have a direct impact on the d' values. The detectability was better with a higher IR level and thicker slice thickness and increment, whereas the VMI keV level made no difference. The d' values mainly increased due to the reduction in noise, since the contrast between the phantom's background and the insert defining each simulated lesion and the spatial resolution showed only a marginal variation. The Br kernel exhibited the highest d', which was expected given its established use for nodule detection [10, 57, 64]. Conversely, the Bl and Qr kernels are typically utilized for quantification of nodules and hence do not require a high d' value. The PC-CT attained higher d' values across all scan modes, in comparison to the EID-CT. Likewise, Si-Mohammed et al. [65] demonstrated a higher image quality and d' with PC-CT compared with EID-CT for GGN and solid nodules.

As reported beforehand, the NPS and TTF results obtained in this study may not precisely reflect the actual capabilities of the scanner, and can potentially impact the accuracy of the computed d' values as well.

4.2. CLINICAL IMPLICATIONS & FUTURE RESEARCH

The results may have important clinical implications, particularly in the context of high-resolution imaging applications such as cardiac and lung imaging, where the ability to resolve small details is crucial for accurate diagnosis and treatment planning. In addition to lung cancer, this population is at a higher risk of chronic obstructive pulmonary disease (COPD) and coronary artery disease (CAD), also called the 'Big 3' (B3). Quantification of CT imaging biomarkers such as lung density and bronchial wall thickness may allow early detection of COPD [66, 67]. Dunning et al. [22] showed improved airway wall thickness measurements with UHR PC-CT. A low-dose chest CT for lung cancer screening encompasses the heart in its field of view, providing an opportunity for evaluating CAD as well. Si-Mohamed at al. [68] demonstrated coronary CT angiography with a PC-CT system improved image quality and diagnostic confidence compared with an EID-CT. In future, one low-dose PC-CT image acquisition may allow the most accurate evaluation of all B3 imaging biomarkers.

The present study demonstrates that PC-CT holds promise for ultra-low dose lung cancer screening while maintaining diagnostic accuracy. To improve upon the current findings, a new anthropomorphic phantom is being developed to better resemble human lungs. PC-CT has demonstrated that reducing the dose to 0.20 mGy (25% dose) does not compromise sensitivity while maintaining a specificity of 75%. Moreover, nodules ranging from 3 to 5 mm in size represent a critical area where sensitivity tends to decrease. Therefore, it is recommended that the primary focus of further studies should be on dose reductions down to 0.2 mGy and nodules of 3-5 mm, using the improved anthropomorphic phantom. Additionally, optimal scan settings from the task-based image quality assessment, such as the UHR Q+ mode with the

highest d' value, should be validated in future anthropomorphic phantom studies.

While the volumetric performance of PC-CT at lower doses was part of the full study, the results were not yet finalized. Dunning et al. [22] conducted a study on the accuracy of pulmonary nodule volume measurement using PC-CT in UHR mode, where they found that the volume error was smaller for PC-CT in the case of spiculated solid and ground-glass nodules (GGN), and remained robust even with dose reduction. They further reported that a sharper kernel (Qr89) on the PC-CT improved the volume accuracy compared to a medium kernel (Qr56) or EID-CT. Therefore, it is interesting to see whether similar findings can be obtained in the forthcoming results, examining whether PC-CT volumetry outcomes surpass those of EID-CT even at reduced doses. Additionally, exploring the potential advantages of using sharper kernels (Qr76-89) and different UHR scan modes for volumetry analysis.

Unfortunately, the effect of different matrix sizes on image quality could not be evaluated in the present study. Nonetheless, Bartlett et al. [63] demonstrated that the use of a 1024 matrix reconstruction in high-resolution PC-CT imaging (at a dose of 13 mGy) enhanced visualization of fine lung structures compared to conventional high-resolution EID-CT. Subsequent studies may explore the feasibility of a 1024 matrix reconstruction in low-dose lung cancer screening in comparison to conventional 512 matrix reconstruction.

4.3. LIMITATIONS

This study has several limitations. Although the Lungman phantom provides a realistic simulation of human lung structure, it is not a perfect representation of clinical practice. The phantom lungs were reported to be more dense and complex than actual human lungs, making detection of nodules more challenging and requiring a learning curve. Additionally, the placement of nodules was limited to lung structures, and nodules could not be placed in mid-air, potentially affecting the applicability of the results to standard clinical conditions. The dose was solely reduced on the PC-CT, limiting the comparability to EID-CT at equivalent dose levels. In future the performance of both PC-CT and EID-CT systems at similar ultra-low dose levels should be compared. The d' evaluation in this study was limited to only two task functions, which may not capture the full range of tasks required in clinical practice. Finally, a QA phantom was used to assess the performance of the imaging system, and the results may not fully reflect its performance when imaging actual patients. Nonetheless, a noteworthy strength of the study is the use of an objective evaluation method, iQMetrix-CT, to assess image quality. Compared to subjective methods, such as the Likert-scale, this approach enhances the reliability and validity of the results. However, it is advisable to validate the findings using an alternative task-based image quality assessment software, such as imQuest [69], given the concerns regarding the iQMetrix-CT outcomes. This additional verification step will provide a more robust and reliable evaluation of the image quality.

5

CONCLUSION

Taken together, these results show that PC-CT is a promising alternative to EID-CT for low dose lung cancer screening, providing a potential solution to the challenges associated with radiation exposure in screening programs, without compromising detection sensitivity or image quality. For early lung cancer detection, attention has to be paid to FP findings at ultra-low dose levels (≃0.1 mGy), leading to unnecessary diagnostic tests and invasive procedures, since the specificity decreased with every dose reduction. Future research will focus on evaluating (ultra-)low radiation doses on both EID-CT and PC-CT to compare their performance in terms of lung nodule detection and volumetry. This evaluation will be conducted using an improved anthropomorphic phantom, which will enhance the accuracy and reliability of the obtained results.

Furthermore, PC-CT improved detectability of simulated pulmonary nodules compared to EID-CT at an equivalent dose, through enhanced image quality and less noise. Although the PC-CT showed similar spatial resolution to the EID-CT, the forthcoming volumetry results and additional verification with other task-based image quality assessment software will provide a more robust and reliable evaluation of the spatial resolution of PC-CT. Future research should focus on validating the optimal acquisition and reconstruction parameters for lung nodule detection, particularly following dose optimization, in both phantoms and patients.

REFERENCES

[1] H. Sung et al. “Global Cancer Statistics 2020: GLOBOCAN Estimates of Incidence and Mortality Worldwide for 36 Cancers in 185 Countries”. In: *CA Cancer J Clin* 71.3 (2021), pp. 209–249. ISSN: 1542-4863 (Electronic)0007-9235 (Linking). DOI: 10.3322/caac.21660. URL: https://www.ncbi.nlm.nih.gov/pubmed/33538338.

[2] N Howlader. “Seer cancer statistics review, 1975-2008, national cancer institute, bethesda, md”. In: *http://seer. cancer. gov/csr/1975_2008/, based on November 2010 SEER data submission, posted to the SEER web site* (2011).

[3] Renée Manser et al. “Screening for lung cancer”. In: *Cochrane database of systematic reviews* 6 (2013).

[4] Glen A Lillington and Cynthia I Caskey. “Evaluation and management of solitary and multiple pulmonary nodules.” In: *Clinics in chest medicine* 14.1 (1993), pp. 111–119.

[5] Dong Ming Xu et al. “Limited value of shape, margin and CT density in the discrimination between benign and malignant screen detected solid pulmonary nodules of the NELSON trial”. In: *European journal of radiology* 68.2 (2008), pp. 347–352.

[6] H. J. de Koning et al. “Reduced Lung-Cancer Mortality with Volume CT Screening in a Randomized Trial”. In: *N Engl J Med* 382.6 (2020), pp. 503–513. ISSN: 1533-4406 (Electronic)0028-4793 (Linking). DOI: 10.1056/NEJMoa1911793. URL: https://www.ncbi.nlm.nih.gov/pubmed/31995683.

[7] Team National Lung Screening Trial Research et al. “Reduced lung-cancer mortality with low-dose computed tomographic screening”. In: *N Engl J Med* 365.5 (2011), pp. 395–409. ISSN: 1533-4406 (Electronic)0028-4793 (Linking). DOI: 10.1056/NEJMoa1102873. URL: https://www.ncbi.nlm.nih.gov/pubmed/21714641.

[8] M. A. Heuvelmans and M. Oudkerk. “Appropriate screening intervals in low-dose CT lung cancer screening”. In: *Transl Lung Cancer Res* 7.3 (2018), pp. 281–287. ISSN: 2218-6751 (Print)2218-6751 (Linking). DOI: 10.21037/tlcr.2018.05.08. URL: https://www.ncbi.nlm.nih.gov/pubmed/30050766.

[9] D. E. Wood et al. “Lung Cancer Screening, Version 3.2018, NCCN Clinical Practice Guidelines in Oncology”. In: *J Natl Compr Canc Netw* 16.4 (2018), pp. 412–441. ISSN: 1540-1413 (Electronic) 1540-1405 (Linking). DOI: 10.6004/jnccn.2018.0020. URL: https://www.ncbi.nlm.nih.gov/pubmed/29632061.

[10] Y. Du et al. “Lung cancer screening with low-dose CT: Simulating the effect of starting screening at a younger age in women”. In: *Eur J Radiol* 148 (2022), p. 110182. ISSN: 1872-7727 (Electronic) 0720-048X (Linking). DOI: 10.1016/j.ejrad.2022.110182. URL: https://www.ncbi.nlm.nih.gov/pubmed/35121333.

[11] Y. Du et al. “Cost-effectiveness of lung cancer screening with low-dose computed tomography in heavy smokers: a microsimulation modelling study”. In: *Eur J Cancer* 135 (2020), pp. 121–129. ISSN: 1879-0852 (Electronic)0959-8049 (Linking). DOI: 10.1016/j.ejca.2020.05.004. URL: https://www.ncbi.nlm.nih.gov/pubmed/32563896.

[12] K. Perisinakis et al. “Radiation burden and associated cancer risk for a typical population to be screened for lung cancer with low-dose CT: A phantom study”. In: *Eur Radiol* 28.10 (2018), pp. 4370–4378. ISSN: 1432-1084 (Electronic)0938-7994 (Linking). DOI: 10.1007/s00330-018-5373-7. URL: https://www.ncbi.nlm.nih.gov/pubmed/29651767.

[13] A. N. H. Walstra. “Review on (ultra) low-dose CT techniques for lung nodule evaluation: energy integrating CT vs. photon-counting CT”. Literature review. 2022.

[14] T. Ottilinger et al. “Semi-automated volumetry of pulmonary nodules: Intra-individual comparison of standard dose and chest X-ray equivalent ultralow dose chest CT scans”. In: *Eur J Radiol* 156 (2022), p. 110549. ISSN: 1872-7727 (Electronic)0720-048X (Linking). DOI: 10.1016/j.ejrad.2022.110549. URL: https://www.ncbi.nlm.nih.gov/pubmed/36272226.

[15] M. Vonder, M. D. Dorrius, and R. Vliegenthart. “Latest CT technologies in lung cancer screening: protocols and radiation dose reduction”. In: *Transl Lung Cancer Res* 10.2 (2021), pp. 1154–1164. ISSN: 2218-6751 (Print) 2218-6751 (Linking). DOI: 10.21037/tlcr-20-808. URL: https://www.ncbi.nlm.nih.gov/pubmed/33718053.

[16] D. E. Jonas et al. “Screening for Lung Cancer With Low-Dose Computed Tomography: Updated Evidence Report and Systematic Review for the US Preventive Services Task Force”. In: *JAMA* 325.10 (2021), pp. 971–987. ISSN: 1538-3598 (Electronic)0098-7484 (Linking). DOI: 10.1001/jama.2021.0377. URL: https://www.ncbi.nlm.nih.gov/pubmed/33687468.

[17] M. Messerli et al. “Ultralow dose CT for pulmonary nodule detection with chest x-ray equivalent dose - a prospective intra-individual comparative study”. In: *Eur Radiol* 27.8 (2017), pp. 3290–3299. ISSN: 1432-1084 (Electronic)0938-7994 (Linking). DOI: 10.1007/s00330-017-4739-6. URL: https://www.ncbi.nlm.nih.gov/pubmed/28093625.

[18] T. Flohr et al. “Photon-counting CT review”. In: *Phys Med* 79 (2020), pp. 126–136. ISSN: 1724-191X (Electronic)1120-1797 (Linking). DOI: 10.1016/j.ejmp.2020.10.030. URL: https://www.ncbi.nlm.nih.gov/pubmed/33249223.

[19] K. Rajendran et al. “Full field-of-view, high-resolution, photon-counting detector CT: technical assessment and initial patient experience”. In: *Phys Med Biol* 66.20 (2021). ISSN: 1361-6560 (Electronic)0031-9155 (Linking). DOI: 10.1088/1361-6560/ac155e. URL: https://www.ncbi.nlm.nih.gov/pubmed/34271558.

[20] J. R. Rajagopal et al. “Comparison of Low Dose Performance of Photon-Counting and Energy Integrating CT”. In: *Acad Radiol* 28.12 (2021), pp. 1754–1760. ISSN: 1878-4046 (Electronic)1076-6332 (Linking). DOI: 10.1016/j.acra.2020.07.033. URL: https://www.ncbi.nlm.nih.gov/pubmed/32855051.

[21] K. Rajendran et al. “First Clinical Photon-counting Detector CT System: Technical Evaluation”. In: *Radiology* 303.1 (2022), pp. 130–138. ISSN: 1527-1315 (Electronic)0033-8419 (Linking). DOI: 10.1148/radiol.212579. URL: https://www.ncbi.nlm.nih.gov/pubmed/34904876.

[22] Chelsea AS Dunning et al. “Accuracy of Nodule Volume and Airway Wall Thickness Measurement Using Low-Dose Chest CT on a Photon-Counting Detector CT Scanner”. In: *Investigative Radiology* (2022), pp. 10–1097.

[23] Kiyoshi Murata and Norihisa Nitta. *Manual multipurpose chest phantom N1 "lungman"*. URL: https://www.kyotokagaku.com/en/products_data/ph-1_01/.

[24] "AAPM Lung Cancer Screening Protocols 2019". In: (2019). URL: https://www.aapm.org/pubs/CTProtocols/documents/LungCancerScreeningCT.pdf.

[25] Truck By Mail. "Catphan® 500 and 600 Manual". In: *The Phantom Laboratory* (2013).

[26] Marion Lassot-Buys et al. "Task-Based Image Quality Assessment Comparing Classical and Iterative Cone Beam CT Images on Halcyon®". In: *Diagnostics* 13.3 (2023), p. 448.

[27] David C Rotzinger et al. "Task-based model observer assessment of a partial model-based iterative reconstruction algorithm in thoracic oncologic multidetector CT". In: *Scientific reports* 8.1 (2018), p. 17734.

[28] J. Greffier et al. "Comparison of noise-magnitude and noise-texture across two generations of iterative reconstruction algorithms from three manufacturers". In: *Diagn Interv Imaging* 100.7-8 (2019), pp. 401–410. ISSN: 2211-5684 (Electronic)2211-5684 (Linking). DOI: 10.1016/j.diii.2019.04.006. URL: https://www.ncbi.nlm.nih.gov/pubmed/31130375.

[29] J. Greffier et al. "Effect of tin filter-based spectral shaping CT on image quality and radiation dose for routine use on ultralow-dose CT protocols: A phantom study". In: *Diagn Interv Imaging* 101.6 (2020), pp. 373–381. ISSN: 2211-5684 (Electronic)2211-5684 (Linking). DOI: 10.1016/j.diii.2020.01.002. URL: https://www.ncbi.nlm.nih.gov/pubmed/32008994.

[30] J. Greffier, Y. Barbotteau, and F. Gardavaud. "iQMetrix-CT: New software for task-based image quality assessment of phantom CT images". In: *Diagnostic and Interventional Imaging* 103.11 (2022), pp. 555–562.

[31] Ehsan Samei et al. "Performance evaluation of computed tomography systems: summary of AAPM Task Group 233". In: *Medical physics* 46.11 (2019), e735–e756.

[32] Robert S Saunders Jr and Ehsan Samei. "Resolution and noise measurements of five CRT and LCD medical displays". In: *Medical Physics* 33.2 (2006), pp. 308–319.

[33] Brady J McKee et al. "Performance of ACR Lung-RADS in a clinical CT lung screening program". In: *Journal of the American College of Radiology* 13.2 (2016), R25–R29.

[34] PASS 2023. "Confidence Intervals for One-Sample Sensitivity and Specificity - Chapter 273". In: NCSS Statistical Software, pp. 273-1-273–15.

[35] M. M. Woeltjen et al. "Low-Dose High-Resolution Photon-Counting CT of the Lung: Radiation Dose and Image Quality in the Clinical Routine". In: *Diagnostics (Basel)* 12.6 (2022). ISSN: 2075-4418 (Print) 2075-4418 (Linking). DOI: 10.3390/diagnostics12061441. URL: https://www.ncbi.nlm.nih.gov/pubmed/35741251.

[36] D. Graafen et al. "Dose Reduction and Image Quality in Photon-counting Detector High-resolution Computed Tomography of the Chest: Routine Clinical Data". In: *J Thorac Imaging* 37.5 (2022), pp. 315–322. ISSN: 1536-0237 (Electronic)0883-5993 (Linking). DOI: 10.1097/RTI.0000000000000661. URL: https://www.ncbi.nlm.nih.gov/pubmed/35699680.

[37] L. Jungblut et al. "First Performance Evaluation of an Artificial Intelligence-Based Computer-Aided Detection System for Pulmonary Nodule Evaluation in Dual-Source Photon-Counting Detector CT at Different Low-Dose Levels". In: *Invest Radiol* 57.2 (2022), pp. 108–114. ISSN: 1536-0210 (Electronic)0020-9996 (Linking). DOI: 10.1097/RLI.0000000000000814. URL: https://www.ncbi.nlm.nih.gov/pubmed/34324462.

[38] Akitoshi Inoue et al. “Lung Cancer Screening Using Clinical Photon-Counting Detector Computed Tomography and Energy-Integrating-Detector Computed Tomography: A Prospective Patient Study”. In: *Journal of Computer Assisted Tomography* (2022), pp. 10–1097.

[39] Dong Ming Xu et al. “Nodule management protocol of the NELSON randomised lung cancer screening trial”. In: *Lung cancer* 54.2 (2006), pp. 177–184.

[40] Dekel Shlomi et al. “Screening for lung cancer: time for large-scale screening by chest computed tomography”. In: *European Respiratory Journal* 44.1 (2014), pp. 217–238.

[41] Xueqian Xie et al. “Sensitivity and accuracy of volumetry of pulmonary nodules on low-dose 16-and 64-row multi-detector CT: an anthropomorphic phantom study”. In: *European radiology* 23 (2013), pp. 139–147.

[42] G. Gheysens et al. “Detection of pulmonary nodules with scoutless fixed-dose ultra-low-dose CT: a prospective study”. In: *European radiology* 32.7 (2022), pp. 4437–4445. ISSN: 1432-1084 (Electronic). DOI: 10.1007/s00330-022-08584-y. URL: https://pubmed.ncbi.nlm.nih.gov/35238969/.

[43] M. Fujita et al. “Lung cancer screening with ultra-low dose CT using full iterative reconstruction”. In: *Japanese journal of radiology* 35.4 (2017), pp. 179–189. ISSN: 1867-108X (Electronic). DOI: 10.1007/s11604-017-0618-y. URL: https://pubmed.ncbi.nlm.nih.gov/28197820/.

[44] S. Gordic et al. “Ultralow-dose chest computed tomography for pulmonary nodule detection: first performance evaluation of single energy scanning with spectral shaping”. In: *Invest Radiol* 49.7 (2014), pp. 465–73. ISSN: 1536-0210 (Electronic)0020-9996 (Linking). DOI: 10.1097/RLI.0000000000000037. URL: https://www.ncbi.nlm.nih.gov/pubmed/24598443.

[45] G. Milanese et al. “Comparison of ultra-low dose chest CT scanning protocols for the detection of pulmonary nodules: a phantom study”. In: *Tumori* 105.5 (2019), pp. 394–403. ISSN: 2038-2529 (Electronic). DOI: 10.1177/0300891619847271. URL: https://pubmed.ncbi.nlm.nih.gov/31041885/.

[46] P. A. Autrusseau et al. “Radiomics in the evaluation of lung nodules: Intrapatient concordance between full-dose and ultra-low-dose chest computed tomography”. In: *Diagnostic and interventional imaging* 102.4 (2021), pp. 233–239. ISSN: 2211-5684 (Electronic). DOI: 10.1016/j.diii.2021.01.010. URL: https://pubmed.ncbi.nlm.nih.gov/33583753/.

[47] B. Jiang et al. “Deep Learning Reconstruction Shows Better Lung Nodule Detection for Ultra-Low-Dose Chest CT”. In: *Radiology* 303.1 (2022), pp. 202–212. ISSN: 1527-1315 (Electronic). DOI: 10.1148/radiol.210551. URL: https://pubmed.ncbi.nlm.nih.gov/35040674/.

[48] Kai Ye et al. “A feasibility study of pulmonary nodule detection by ultralow-dose CT with adaptive statistical iterative reconstruction-V technique”. In: *European Journal of Radiology* 119 (2019), p. 108652.

[49] K Ye et al. “Ultra-low-dose CT reconstructed with ASiR-V using SmartmA for pulmonary nodule detection and Lung-RADS classifications compared with low-dose CT”. In: *Clinical Radiology* 76.2 (2021), 156–e1.

[50] T. Sartoretti et al. “Quantum Iterative Reconstruction for Low-Dose Ultra-High-Resolution Photon-Counting Detector CT of the Lung”. In: *Diagnostics (Basel)* 12.2 (2022). ISSN: 2075-4418 (Print)2075-4418 (Linking). DOI: 10.3390/diagnostics12020522. URL: https://www.ncbi.nlm.nih.gov/pubmed/35204611.

[51] S. Si-Mohamed et al. “Feasibility of lung imaging with a large field-of-view spectral photon-counting CT system”. In: *Diagn Interv Imaging* 102.5 (2021), pp. 305–312. ISSN: 2211-5684 (Electronic)2211-5684 (Linking). DOI: 10.1016/j.diii.2021.01.001. URL: https://www.ncbi.nlm.nih.gov/pubmed/33610503.

[52] J Greffier et al. “CT iterative reconstruction algorithms: a task-based image quality assessment”. In: *European radiology* 30 (2020), pp. 487–500.

[53] Lifeng Yu, Shuai Leng, and Cynthia H McCollough. “Dual-energy CT–based monochromatic imaging”. In: *American journal of Roentgenology* 199.5_supplement (2012), S9–S15.

[54] Katharine L Grant et al. “Assessment of an advanced image-based technique to calculate virtual monoenergetic computed tomographic images from a dual-energy examination to improve contrast-to-noise ratio in examinations using iodinated contrast media”. In: *Investigative radiology* 49.9 (2014), pp. 586–592.

[55] K Eldevik, W Nordhøy, and A Skretting. “Relationship between sharpness and noise in CT images reconstructed with different kernels”. In: *Radiation protection dosimetry* 139.1-3 (2010), pp. 430–433.

[56] Muhammad Shafiq-ul-Hassan et al. “Accounting for reconstruction kernel-induced variability in CT radiomic features using noise power spectra”. In: *Journal of Medical Imaging* 5.1 (2018), pp. 011013–011013.

[57] R. Symons et al. “Low-dose lung cancer screening with photon-counting CT: a feasibility study”. In: *Phys Med Biol* 62.1 (2017), pp. 202–213. ISSN: 1361-6560 (Electronic)0031-9155 (Linking). DOI: 10.1088/1361-6560/62/1/202. URL: https://www.ncbi.nlm.nih.gov/pubmed/27991453.

[58] Z. Yu et al. “Noise performance of low-dose CT: comparison between an energy integrating detector and a photon counting detector using a whole-body research photon counting CT scanner”. In: *J Med Imaging (Bellingham)* 3.4 (2016), p. 043503. ISSN: 2329-4302 (Print) 2329-4302 (Linking). DOI: 10.1117/1.JMI.3.4.043503. URL: https://www.ncbi.nlm.nih.gov/pubmed/28018936.

[59] Steven Dolly et al. “Practical considerations for noise power spectra estimation for clinical CT scanners”. In: *Journal of applied clinical medical physics* 17.3 (2016), pp. 392–407.

[60] Ki Hyun Lee et al. “Detection of blebs and bullae in patients with primary spontaneous pneumothorax by multi-detector CT reconstruction using different slice thicknesses”. In: *Journal of Medical Imaging and Radiation Oncology* 58.6 (2014), pp. 663–667.

[61] Wieying Kuo et al. “Multicentre chest computed tomography standardisation in children and adolescents with cystic fibrosis: the way forward”. In: *European Respiratory Journal* 47.6 (2016), pp. 1706–1717.

[62] Shuai Leng et al. “150-μm spatial resolution using photon-counting detector computed tomography technology: technical performance and first patient images”. In: *Investigative radiology* 53.11 (2018), pp. 655–662.

[63] David J Bartlett et al. “High-resolution chest CT imaging of the lungs: Impact of 1024 matrix reconstruction and photon-counting-detector CT”. In: *Investigative radiology* 54.3 (2019), p. 129.

[64] M. P. Revel. *Chest CT for Lung Cancer Screening - Technical standards*. Web Page. 2020. URL: https://www.myesti.org/content-esti/uploads/ESTI-LCS-technical-standards_2019-06-14.pdf.

[65] Salim A Si-Mohamed et al. “Comparison of image quality between spectral photon-counting CT and dual-layer CT for the evaluation of lung nodules: A phantom study”. In: *European Radiology* 32 (2022), pp. 524–532.

[66] Onno M Mets et al. “Diagnosis of chronic obstructive pulmonary disease in lung cancer screening computed tomography scans: independent contribution of emphysema, air trapping and bronchial wall thickening”. In: *Respiratory research* 14 (2013), pp. 1–8.

[67] Akkelies E Dijkstra et al. “Novel genes for airway wall thickness identified with combined genome-wide association and expression analyses”. In: *American journal of respiratory and critical care medicine* 191.5 (2015), pp. 547–556.

[68] Salim A Si-Mohamed et al. “Coronary CT angiography with photon-counting CT: first-in-human results”. In: *Radiology* 303.2 (2022), pp. 303–313.

[69] J Solomon et al. “An automated software tool for task-based image quality assessment and matching in clinical CT using the TG-233 Framework”. In: *Medical Physics*. Vol. 45. 6. WILEY 111 RIVER ST, HOBOKEN 07030-5774, NJ USA. 2018, E134–E134.

ACKNOWLEDGEMENTS

This thesis was made possible by the collaboration, support and advice of many people.

First and foremost, I wish to express my sincere appreciation to my supervisors for their guidance and support throughout. I am grateful to Rozemarijn Vliegenthart, whose expertise in the field of cardiothoracic radiology has been invaluable throughout this project. Thank you for the warm welcome to UMC Groningen and for providing me with an interesting and diverse clinical program. My gratitude also goes to Marcel van Straten for his technical support and critical eye. The insights and feedback have challenged me and contributed to improving the quality of the thesis. I thank Marcel Greuter for his technical expertise and consistently positive attitude, as well as his warm welcome to Groningen, along with Joost Hop. I would like to express my appreciation to Niels Schurink for his supervision and guidance throughout the thesis process. His mentorship has played a role in making my time at Siemens Healthineers an enjoyable experience.

My gratitude goes out to Theo van Walsum from the Erasmus MC, for stepping in at short notice to act as chair, and to Wouter Veldkamp from the LUMC for contributing his expertise to the committee.

Joost, I am grateful for our extensive collaboration on the study and for making the late evenings when we conducted the phantom tests more fun. Moreover, I would like to acknowledge both Niels and Joost for the trip to Forchheim and their help with the phantom scans, as well as the fun dinners and German beers that we shared.

My appreciation also goes to Sebastian Faby for his invaluable assistance during our time in Forchheim. His support made the phantom tests run smoothly, and his technical expertise and insights were immensely helpful throughout the thesis process. I extend my gratitude to Dave Douwes for his assistance with the NAEOTOM Alpha simulator, which facilitated the smooth execution of the phantom tests in Forchheim.

A further thank you goes to Siemens Healthineers and the radiology department at UMC Groningen, for making this project possible and giving me the opportunity to work with such innovative technology. I am also grateful to the group of colleagues from Siemens Healthineers for making the experience of working at the office in the Hague such fun.

A special thank you goes to Saskia, Jeroen, Merith, Mare and Nienke for letting me stay with you in Zuidhorn during the weeks I needed to be at the UMC Groningen, and making me feel so welcome and at home. I thoroughly enjoyed the dinners and evenings on the couch getting to know you all better.

I would also like to thank my friends for their support, working together, sharing countless cups of coffee, and being a part of this thesis journey with me. Your presence made the process much more enjoyable.

To my family, thank you for your constant support and encouragement leading up to this moment. I am especially grateful to my parents, on whom I can always count for advice, guidance and free meals when needed.

Last but not least, I would like to thank Youri for his love and support, offering fun distractions and comfort food whenever I needed them. Your presence made the whole experience much more pleasant and fulfilling.

APPENDIX

A. NODULE PLACEMENT SCHEME

PC-CT

Scannummer	Nodules											
	L	R	L	R	L	R	L	R	L	R	L	R
1	15	20	9	30	19	11	10					
2	34	17	33	29	36	4	28					
3	23	26	30	22	21	11	34					
4	20	9	14	33								
5	16	30	28	22								
6	15	14	23	8	17							
7	5	6	8	24	33	10	31	27	14	3		
8	2	5	26	10	36	12	25	16	1	24	13	27
9	3	36	22	12	6							
10	13	21	23	31	32	7	35	28	25			
11	18	32	5	24	13	19	4					
12	12	20	29	21	11	2	16	7	35			
13	4	1										
14	32	35	8	26	18	34	3					
15	25	17	15	2	1							
16	18	19	6	31	7	29	9	27				

Figure A.1: Automatically generated scheme for the placement of the simulated nodules in the Lungman phantom. (L, left lung; R, right lung)

EID-CT

Scannummer	Nodules											
	L	R	L	R	L	R	L	R	L	R	L	R
1	25	20	12	15	36	2						
2	3	34	21	10	16	33						
3	7	18	31	36	25	22	4					
4	34	1	18	5	12	24						
5	19	14	10	22	9	13						
6	27	7	32	2	17	21	36	23	24			
7	21	19	15	24	12	11	29	8	26	4	33	18
8	6	13	17	20	31	15	8	1				
9	16	29	34	5	25	28	32					
10	32	8	23	30								
11	2	35	27	22	13	9	3					
12	28	6	31	3	7	26	35					
13	26	9	33	27	1							
14	4	30	11	10	17	29	14	16	28			
15	14	5	11	6	35							
16	20	19	30									

Figure A.2: Automatically generated scheme for the placement of the simulated nodules in the Lungman phantom. (L, left lung; R, right lung)

SIMULATED NODULES NUMBERED

Figure A.3: Overview of the artificial nodules, numbered accordingly.

B. NODULE DETECTION SENSITIVITY

SHAPE AND DENSITY

Table B.1: Pulmonary nodule sensitivity specifically for each shape and density. (HU, Hounsfield Unit; EID, Energy-Integrating Detector; PC, Photon-Counting)

Reader 1 (GJ)	**Density**		**Shape**		
	100 HU	-300 HU	Sphere	Lobulated	Spiculated
EID	67%	52%	64%	56%	58%
PC 100%	63%	54%	56%	50%	69%
PC 75%	65%	54%	56%	50%	72%
PC 50%	67%	57%	58%	56%	72%
PC 25%	56%	56%	58%	44%	64%
PC 10%	52%	52%	50%	44%	61%

Pulmonary Nodule Detection

Table B.2: Pulmonary nodule detection results of reader 1 and the corresponding sensitivity. Nodule numbers refer to figure A.3.

	Nodule				Reader 1 (GJ)											
#	Shape	HU	d (mm)	Present	EID-CT	Sensitivity	PCD (100%)	Sensitivity	PCD (75%)	Sensitivity	PCD (50%)	Sensitivity	PCD (25%)	Sensitivity	PCD (10%)	Sensitivity
1	Sphere	100	2.5	18		0%		0%		0%		0%		0%		0%
2	Sphere	100	3	18	3	100%		0%		0%		0%		0%		0%
3	Sphere	100	4	18	2	67%	1	33%	3	100%	2	67%	2	67%	2	67%
4	Sphere	100	5	18	3	100%	3	100%	3	100%	3	100%	3	100%	2	67%
5	Sphere	100	6	18	3	100%	3	100%	3	100%	3	100%	3	100%	3	100%
6	Sphere	100	10	18	3	100%	3	100%	3	100%	3	100%	3	100%	2	67%
7	Sphere	-300	2.5	18		0%		0%		0%		0%		0%		0%
8	Sphere	-300	3	18		0%		0%		0%		0%		0%		0%
9	Sphere	-300	4	18		0%	1	33%		0%	1	33%	1	33%	1	33%
10	Sphere	-300	5	18	3	100%	3	100%	3	100%	3	100%	3	100%	2	67%
11	Sphere	-300	6	18	3	100%	3	100%	2	67%	3	100%	3	100%	3	100%
12	Sphere	-300	10	18	3	100%	3	100%	3	100%	3	100%	3	100%	3	100%
13	Lobulated	100	2.5	18		0%		0%		0%		0%		0%		0%
14	Lobulated	100	3	18		0%		0%		0%		0%		0%		0%
15	Lobulated	100	4	18	2	67%	1	33%	2	67%	3	100%		0%		0%
16	Lobulated	100	5	18	3	100%	3	100%	2	67%	2	67%	1	33%	2	67%
17	Lobulated	100	6	18	3	100%	3	100%	3	100%	3	100%	3	100%	3	100%
18	Lobulated	100	10	18	3	100%	3	100%	3	100%	3	100%	3	100%	3	100%
19	Lobulated	-300	2.5	18		0%		0%		0%		0%		0%		0%
20	Lobulated	-300	3	18		0%		0%		0%		0%		0%		0%
21	Lobulated	-300	4	18		0%		0%		0%		0%		0%		0%
22	Lobulated	-300	5	18	3	100%	2	67%	2	67%	3	100%	3	100%	2	67%
23	Lobulated	-300	6	17	2*	100%	3	100%	3	100%	3	100%	3	100%	3	100%
24	Lobulated	-300	10	18	3	100%	3	100%	3	100%	3	100%	3	100%	3	100%
25	Spiculated	100	2.5	18		0%	1	33%		0%	1	33%		0%		0%
26	Spiculated	100	3	18	1	33%	1	33%	1	33%	1	33%		0%		0%
27	Spiculated	100	4	18	3	100%	3	100%	3	100%	3	100%	3	100%	2	67%
28	Spiculated	100	5	18	2	67%	3	100%	3	100%	3	100%	3	100%	3	100%
29	Spiculated	100	6	13	2	67%	2*	100%	2*	100%	2*	100%	2*	100%	2*	100%
30	Spiculated	100	10	18	3	100%	3	100%	3	100%	3	100%	3	100%	3	100%
31	Spiculated	-300	2.5	18		0%		0%		0%		0%	1	33%		0%
32	Spiculated	-300	3	18		0%	1	33%	2	67%	1	33%		0%	1	33%
33	Spiculated	-300	4	18	2	67%	1	33%	2	67%	2	67%	1	33%	2	67%
34	Spiculated	-300	5	18	2	67%	3	100%	3	100%	3	100%	3	100%	2	67%
35	Spiculated	-300	6	18	3	100%	3	100%	3	100%	3	100%	3	100%	3	100%
36	Spiculated	-300	10	18	3	100%	3	100%	3	100%	3	100%	3	100%	3	100%

*Nodule scanned only twice, instead of the standard three times
EID, energy-intergrating detector; PCD, photon-counting detector; HU, Hounsfield Unit

C. EDGE SPREAD FUNCTION FIT

COEFFICIENT OF DETERMINATION (R^2)

Table C.1: The R^2 value to quantitatively evaluate the goodness-of-fit of the ESF curves to the raw data. Due to the requirement of repeating the calculations to obtain the raw ESF data, the R^2 was computed exclusively for the three standard reconstruction kernels of both CT systems, as well as for scans exhibiting atypical TTF curves.

CT series	R2 Delrin	R2 Teflon
EID-CT (Sn)		
Br40	0.997	0.993
Bl57	0.967	0.982
Qr59	0.975	0.994
PC-CT		
(QSn) Br40	0.992	0.998
(QSn) Bl56	0.960	0.997
(QSn) Qr60	0.979	0.999
(UHR QSn) Qr60	0.997	0.999
(UHR Q+) Qr60	0.998	0.978

ESF FIT EXAMPLE

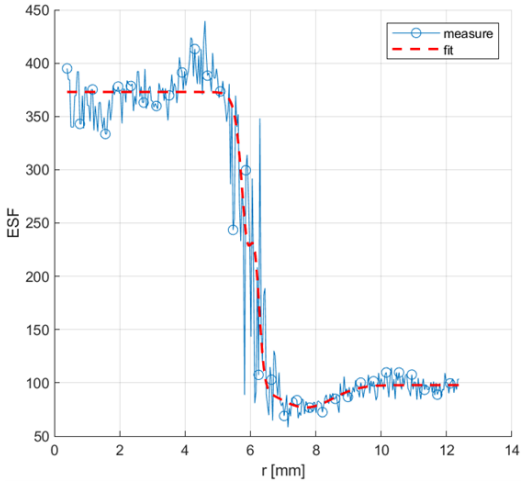

Figure C.1: ESF raw and fitted curve of the PC-CT in QSn mode and Bl56 kernel of the Delrin insert, illustrating the fit with the lowest observed R^2 in table C.1. The fit of the edge beginning, *i.e.* the beginning of the curve decline, is oversimplified compared to t he raw data.

D. NOISE POWER SPECTRUM RAW DATA

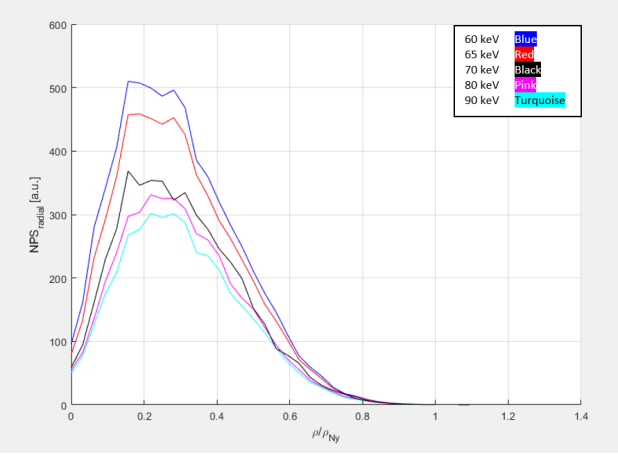

Figure D.1: Noise Power Spectrum (NPS) calculation with in-house software of Siemens Healthineers with image subtraction as background removal method, to evaluate the impact of the second order polynomial fit to remove background noise in the iQMetrix-CT software.

E. MODULATION TRANSFER FUNCTION

Table E.1: MTF values determined by Siemens Healthineers for the two detector systems and the kernels that were used for reference reconstruction.

	EID-CT			
Kernel	MTF-50 [1/cm]	MTF_10 [1/cm]	MTF_4 [1/cm]	MTF_2 [1/cm]
Br40	4.0	6.4	7.3	7.8
Bl57	7.7	9.2	9.8	10.2
Qr59	8.3	13.4	13.9	14.2
	PC-CT (144 x 0.4 mm)			
Kernel	MTF-50 [1/cm]	MTF_10 [1/cm]	MTF_4 [1/cm]	MTF_2 [1/cm]
Br40	4.0	6.4	7.3	7.8
Bl56	7.5	9.0	9.6	10.0
Qr60	8.8	11.2	11.5	11.6